Journal of Materials Chemistry A

ROYAL SOCIETY OF CHEMISTRY

REVIEW

View Article Online
View Journal | View Issue

Cite this: J. Mater. Chem. A, 2020, 8, 2875

A materials perspective on magnesium-ion-based solid-state electrolytes

Prem Wicram Jaschin, [a] Yirong Gao,[a] Yao Li*[b] and Shou-Hang Bo *[a]

As economically viable alternatives to lithium-ion batteries, magnesium-ion-based all-solid-state batteries have been researched to meet the criteria for an ideal energy storage device. With an energy-dense magnesium-metal anode, such batteries can provide almost double the volumetric energy density at half the cost when compared with that obtainable from the state-of-the-art lithium-ion batteries. Although the development of solid-state magnesium-based batteries is hindered by various factors, the identification of an appropriate electrolyte remains the most challenging and limiting factor. In this review, we provide a survey of inorganic ceramic, metal–organic framework, glass, and organic solid polymer electrolytes that have been developed till date. We discuss the relationship between the structure, composition, and ionic conductivity of these inorganic Mg^{2+}-ion solid-state electrolytes as well as the fundamental Mg-ion conduction mechanisms that govern magnesium transport in these solids, emphasizing on Mg^{2+}-ion-conducting inorganic materials. By a comparison of Mg^{2+}- and Na^{+}-ion conductors under the theoretical framework of multi-excitation entropy (or Meyer–Neldel rules), we highlight the possible differences between these two systems, which can yield substantially different ion transport characteristics.

Received 24th October 2019
Accepted 7th January 2020

DOI: 10.1039/c9ta11729f

rsc.li/materials-a

1. Introduction

Energy technology is in a state of transition, weaning away from fossil fuels as the energy source and embracing alternative, green sources such as solar and wind power. The intermittent availability of solar and wind energy limits the power-on-demand necessity for applications such as electrical grids. This drawback may be addressed by storing energy, whenever available, in batteries and tapping it when required. Similarly, the automotive sector is shifting gears toward electric energy for a more sustainable and pollution-free world.[1–8] Thus, there is an urgent need to explore battery systems with higher energy

[a]University of Michigan-Shanghai Jiao Tong University Joint Institute, Shanghai Jiao Tong University, 800 Dong Chuan Road, Minhang District, Shanghai 200240, China. E-mail: shouhang.bo@sjtu.edu.cn; Fax: +86-21-34206525; Tel: +86-21-34206765

[b]State Key Laboratory of Metal Matrix Composites, Shanghai Jiao Tong University, 800 Dong Chuan Road, Minhang District, Shanghai 200240, China. E-mail: liyaosjtu@sjtu.edu.cn; Fax: +86-21-54745834; Tel: +86-21-34202749

Prem Wicram Jaschin received his MSc in Materials Science from Anna University, India. In 2018, he completed his PhD in Materials Science from the Indian Institute of Science, India, under the supervision of Prof. K. B. R. Varma. Then, he joined Dr Shou-Hang Bo's group as a postdoctoral fellow at the University of Michigan-Shanghai Jiao Tong University Joint Institute, China. His current research focuses on the application of glass–ceramic materials as solid-state electrolytes and electrode–solid-electrolyte interface engineering.

Yirong Gao obtained her BS in 2014 from the Department of Materials Science and Engineering, Central South University of Forestry and Technology, China. She received her MS in Materials Engineering from the Wuhan University of Technology in 2017. Now, she is a PhD candidate at Shanghai Jiao Tong University under the supervision of Dr Shou-Hang Bo. Her research focuses on the ion transport mechanism in lithium superionic conductors.

densities and lower cost than present-day lithium-ion batteries in which graphite and lithium cobalt oxide are used as the anode and cathode, respectively.[9–12] However, lithium-metal-based batteries still remain a far cry due to safety concerns arising from the intrinsic instability of the lithium anode.[13–20] Lithium metal is highly reactive against liquid electrolytes and forms protrusions instead of smooth deposits during cycling, which can lead to a substantial reduction in cycling efficiency and even short circuit in the battery. Although we have witnessed the discovery of high-voltage cathodes[21–23] and notable advances toward the stable cycling of lithium-metal anodes in the recent years,[24–26] resolving this limitation is still formidable;[27] therefore, alternative anodes—particularly those based on tin and silicon—should be investigated.[28–36] There is hope, however, in the form of magnesium, the diagonal alkaline earth neighbor of lithium in the periodic table, which is waiting to be explored.

Magnesium is the fifth most abundant metal in the earth's crust,[37,38] accounting for about 2.1% of the earth's mass, and it is inexpensive and environmentally friendly. Moreover, with an equivalent weight of 12.15 g mol^{-1} and a theoretical density of 1.738 g cm^{-3}, magnesium can deliver theoretical specific capacities of 2233 mA h g^{-1} and 3832 mA h cm^{-3} as compared to the respective values for lithium, namely, 3862 mA h g^{-1} and 2061 mA h cm^{-3} (equivalent weight: 6.94 g mol^{-1}; density: 0.53 g cm^{-3}). Therefore, in principle, batteries based on energy-dense magnesium metal can achieve even higher volumetric energy densities than those obtained from lithium-based batteries. Moreover, and most importantly, a magnesium anode is much less susceptible to dendrite formation than a lithium anode.[39,40] Based on a series of electrodeposition characteristics of magnesium metal, Matsui[40] concluded that the absence of a solid-electrolyte interphase (SEI) layer and high coulombic efficiency resulted in the uniform deposition of magnesium metal, restraining any dendrite formation. These results were further corroborated by density functional theory (DFT) calculations, as performed by Ling *et al.*,[41] who attributed the preferred crystalline-layered deposition of magnesium to the strong Mg–Mg bond induced by the large free energy difference between the higher- and lower-dimensional depositions of magnesium. Recently, although magnesium metal has been shown to form dendrites during electrochemical deposition at a current density of 0.92 mA cm^{-2} and cycling duration of 8 h,[42] whether magnesium will remain problematic under practical cycling conditions (*e.g.*, areal energy density < 5 mA h cm^{-2}; the use of a separator under electrolyte-lean condition) or not is still an open question.

The realization of a practical magnesium-based battery stills rests on several technical challenges. The paucity of suitable cathodes and electrolytes, as well as sluggishness of magnesium anode kinetics, is on the top of the list. Serious efforts at identifying a cathode-active material for use in magnesium-based batteries began with the work of Gregory *et al.*,[43] who proposed ZrS_2, Co_3O_4, and RuO_2 as possible intercalation cathodes. Since then, a host of materials have been examined for reversible magnesium intercalation, such as semiconducting $(Mg_{1-x}Co_x)(Mg_{1-y}Co_y)O_4$;[44] disordered spinel $Mg_{0.67}Ni_{1.33}O_2$;[45] V_2O_5 xerogel;[45,46] Chevrel-phase Mo_6S_8;[47] graphene-like MoS_2;[48–50] and "post-spinel" $MgMn_2O_4$,[51] Ti_2S_4,[52] and $Mg_{1.03}Mn_{0.97}SiO_4$.[53] The challenge lies in fabricating a host that permits fast Mg^{2+} transport kinetics. However, the divalent nature of Mg^{2+} can lower the diffusion rate due to stronger bonding to the host structure when compared with those of monovalent Li^+ and Na^+. As elaborated below, this poses a fundamental challenge for finding solid-state magnesium-ion electrolytes that permit facile Mg^{2+} diffusion at room temperature.

Electrolyte, a key constituent of Mg-ion batteries, also appears to be problematic. The use of liquid electrolytes in magnesium-based batteries is plagued by one or more of the following issues: compatibility of the electrolytes with magnesium metal and high-voltage cathodes, narrow electrochemical

Dr Yao Li received his PhD in Materials Science from the Shanghai Jiao Tong University, China, in 2015. He joined as a research associate at Shanghai Jiao Tong University in 2015. He is working on research related to bioinspired and carbon materials, as well as their applications in energy storage and environmental treatments.

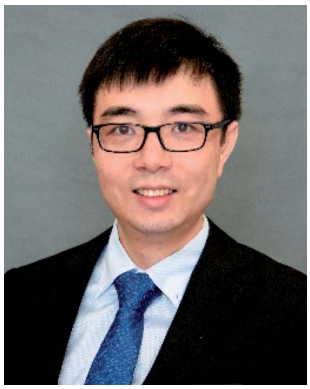

Dr. Shou-Hang Bo received his BS in Chemistry from Fudan University in 2009 and his PhD in Chemistry from Stony Brook University in 2014. Since 2014, Dr Bo has been a postdoctoral fellow at the Department of Materials Science and Engineering, Massachusetts Institute of Technology, and Materials Sciences Division, Lawrence Berkeley National Laboratory. Dr Bo joined the University of Michigan-Shanghai Jiao Tong University Joint Institute in 2017 as a tenure-track assistant professor. His recent research interests include fast ionic conductors for use in solid-state batteries, optimization of the chemical and mechanical properties of solid-state interfaces in batteries, and imaging of solid-state batteries.

stability window, and volatility and corrosive nature of the electrolyte. The low reduction potential of magnesium prevents its plating in aqueous solutions, although whether the reversible plating of magnesium metal can be achieved or not in recently developed water-in-salt electrolytes remains to be explored.[54] The nonaqueous electrochemistry of magnesium is also unique, limiting its reversible deposition from aprotic electrolytes containing salts, such as magnesium perchlorate, magnesium tetrafluoroborate, and magnesium bis(trifluoromethanesulfonyl)imide,[43,55–58] and aprotic solvents, such as carbonates and nitriles.[44,56] Unlike the electronically insulating but ionically conducting SEI formed between the lithium and carbonate electrolytes,[59,60] the passive layer formed by the chemical/electrochemical reactions between magnesium and the electrolyte profoundly influences reversible magnesium deposition as it often blocks the diffusion of Mg^{2+} ions.[43,55] A more comprehensive outlook on liquid electrolytes for magnesium-ion batteries is reported elsewhere, and they are out of the scope of this review.[58,61]

2. Solid electrolytes

All-solid-state batteries have begun to be commercialized for niche applications as they inch their way into everyday lives. Being devoid of liquids, solid-state batteries can ensure higher levels of safety (nonflammability), possess better electrochemical and thermal stabilities, and are leakproof. The absence of or minimal interactions between the electrolyte and active materials would imply a substantially reduced loss of capacity upon storage/cycling and would render the battery useful at elevated temperatures. Unlike liquid electrolytes, where anion migration causes detrimental polarization effects, charge compensation across the solid-state electrolyte only occurs through the diffusion of active ions.

Besides exhibiting high ionic conductivity (of the order of 10^{-3} S cm^{-1}), a solid electrolyte should ideally possess the following properties for better electrochemical performance in an all-solid-state battery: negligible electronic conductivity, single mobile ion species, high transference number (ratio of electric current due to the mobile ion to the total current), wide electrochemical stability window, chemical and thermal stabilities, compatibility with magnesium metal and high-voltage cathodes, high mechanical strength, and ease of processability in addition to being economical, safe, and environmentally friendly. A schematic enumerating the prerequisites of an ideal electrolyte is shown in Fig. 1. Nevertheless, finding an ideal material to satisfy all the above-mentioned attributes is formidable; the optimization of parameters according to specific needs is more viable.

A surge in the number of publications dedicated toward the discovery of novel solid-state magnesium-ion conductors in the last decade (Fig. 2(a)) has indicated that the stage has been set for significantly improved advancements in the field of rechargeable magnesium-based solid-state batteries. In this review, various solid-state material systems that involve Mg^{2+}-ion conduction will be covered, and the properties with respect to their integration with a solid-state battery will be delineated. The materials systems in this review are broadly classified based on polymers and ceramics (Fig. 2(b)). Inorganic polycrystalline ceramics, glasses, and metal–organic frameworks (MOFs) will be covered among the ceramic materials, which will be followed by detailed discussions on the advancements made in the field of solid polymer electrolytes (SPEs) and gel polymer electrolytes (GPEs), as well as ceramic–polymer-based composite electrolytes. In the end, we offer an outlook for further research in the search for an ideal Mg^{2+}-ion-conducting solid-state electrolyte.

2.1. Ceramic-based solid electrolytes

The following sections present discussions on the ionic conductivities associated with various Mg^{2+}-ion solid-state polycrystalline ceramics, which are categorized into inorganic oxides, hydrides, and chalcogenides, as well as MOFs.

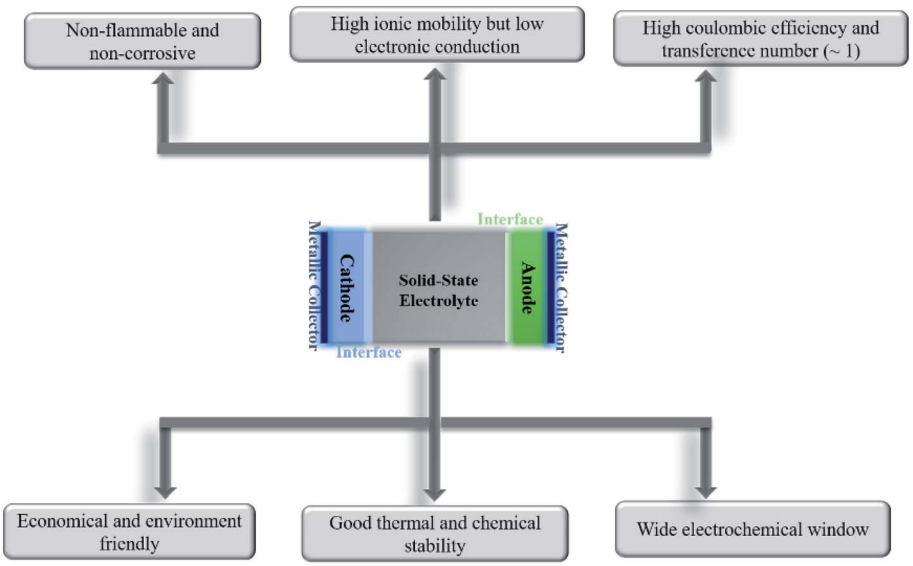

Fig. 1 Schematic of the prerequisites of an ideal solid-state electrolyte.

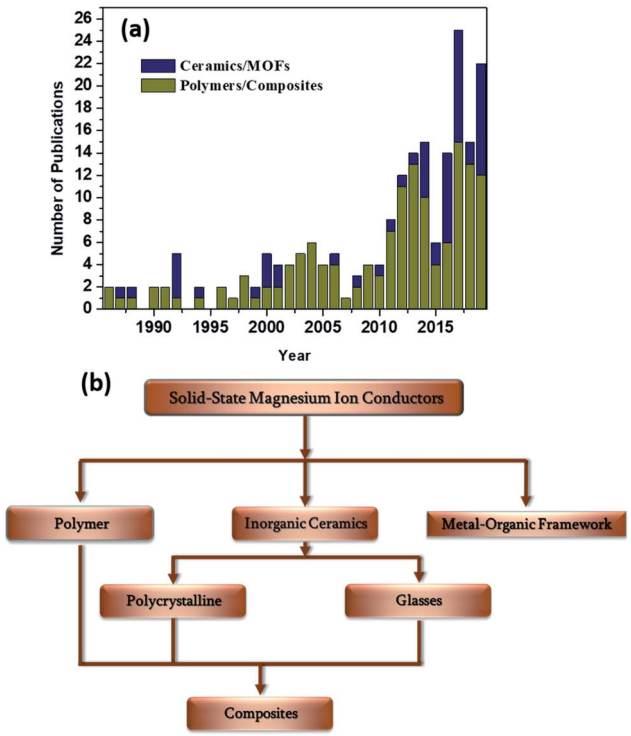

Fig. 2 (a) Plot of the number of publications on solid magnesium-ion conductors investigated over the past few decades and (b) schematic of materials-based categorization of solid-state ionic conductors.

2.1.1. Oxides. The first report on Mg^{2+}-ion-conducting solids appeared in 1987, where Ikeda *et al.*[62] investigated Mg^{2+} conductivity in an Mg–Zr–PO_4 system. The $MgZr_4(PO_4)_6$ composition (*i.e.*, $Mg_{0.5}Zr_2(PO_4)_3$) was shown to exhibit bulk ionic conductivities of 2.9×10^{-5} and 6.1×10^{-3} S cm^{-1}, respectively, at 400 and 800 °C, with activation energy for conduction of 0.82 eV. The fact that Mg^{2+} ions were the charge carriers in this material was confirmed by the Tubandt's method and electron probe microanalysis.[62] The structure of the material was initially indexed to the rhombohedral $R\bar{3}c$ structure, which was the same as that of the $NaZr_2(PO_4)_3$ (NASICON) crystal structure, although a secondary magnesium-deficient phase of zirconium oxyphosphate ($Zr_2O(PO_4)_2$) was also present. Later, Kazakos-Kijowski *et al.*[63] developed a sol–gel route to synthesize pure $Mg_{0.5}Zr_2(PO_4)_3$ and found that the material crystallized in monoclinic $P2_1/n$ symmetry (similar to that in β-Fe_2SO_4) as the rhombohedral phase did not account for certain peaks that occurred in the XRD pattern. A schematic of the crystal structure of $Mg_{0.5}Zr_2(PO_4)_3$, viewed along the *b*-axis is shown in Fig. 3(a). The crystal structure reveals that ionic diffusion occurs across the channels formed by three PO_4 tetrahedra and three ZrO_6 octahedra forming a three-dimensional network of tunnels. The size of these channels (4.5–4.7 Å) is such that they are larger than the edges of magnesium tetrahedra (3.3–3.7 Å).[64] Recently, a sol–gel-processed pure $Mg_{0.5}Zr_2(PO_4)_3$ phase was shown to exhibit better ionic conductivity of 7.23×10^{-3} S cm^{-1} at a relatively lower temperature of 725 °C without a considerable change in the activation energy;[65] this was likely due to the high density (99% of the theoretical density) of ceramic pellets. However, a composite formed by the distribution of a secondary phase of $ZrO(PO_4)_2$ in the parent $Mg_{0.5}Zr_2(PO_4)_3$ ceramic system led to improved ionic conductivity of 6.92×10^{-3} S cm^{-1} at 800 °C for an optimized composition of $Mg_{1.4}Zr_4P_6O_{24.4} + 0.4Zr_2O(PO_4)_2$.[66] This behavior could be attributed to the reduced grain-boundary resistance toward ionic migration due to the presence of a secondary phase. However, the net activation energy of the composite was as high as 1.14 eV, yielding much higher apparent room-temperature ionic conductivity.

Whether the structure is monoclinic or rhombohedral largely determines the ionic conductivity of $Mg_{0.5}Zr_2(PO_4)_3$. In general, materials that are from the NASICON family can crystallize in either the rhombohedral or monoclinic structure, which are associated with the space groups $R\bar{3}c$ and $C2/c$, respectively.[67,68] The rhombohedral structure consists of two distinct sites arranged in a zigzag manner for the conduction of mobile ions (sites 1 and 2). However, the monoclinic structure possesses an additional third site (site 3) as site 2 is split into

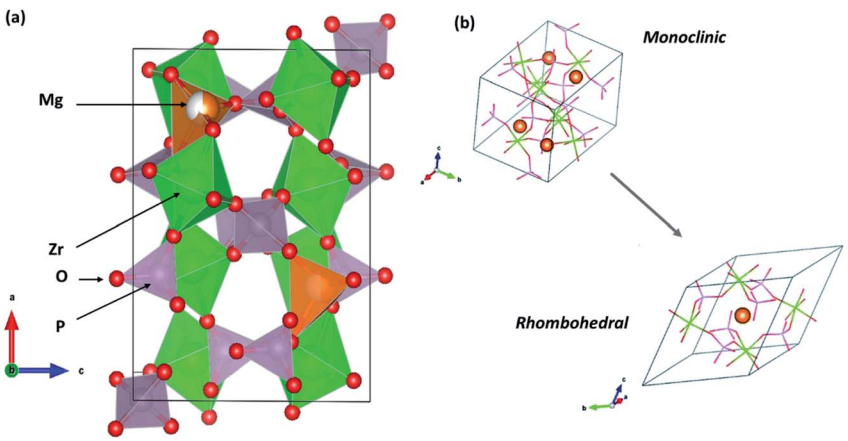

Fig. 3 (a) Crystal structure of $Mg_{0.5}Zr_2(PO_4)_3$ (β-Fe_2SO_4 structure) viewed along its *b*-axis (drawn using VESTA) and (b) its rhombohedral crystal structure variant. Reproduced from ref. 70 with permission, copyright 2019, Royal Society of Chemistry.

two positions in these crystal systems. As a result, the diffusion of mobile species occurs across site 2–1–2 or site 3–1–3. However, the conduction pathway in a monoclinic-structured $Mg_{0.5}Zr_2(PO_4)_3$ is still unclear as the crystal structure varies from that of Na-based NASICON. In addition, NASICON monoclinic structures may exhibit a phase transition at higher temperatures to a rhombohedral structure that can yield more facile mobility of ions due to the concomitant enlargement in the size of the bottleneck (also known as order–disorder transition). In the case of $Mg_{0.5}Zr_2(PO_4)_3$, such a transition is yet to be conclusively proven as the phase transition occurring at 670–680 °C has only been mentioned based on thermal studies without any high-temperature structural data to corroborate the claim.[69] A recent theoretical analysis based on the first-principles molecular dynamics (FPMD) studies comparing the ionic diffusions in monoclinic and rhombohedral crystal structures of $Mg_{0.5}Zr_2(PO_4)_3$ conveys an intriguing aspect.[70] The centrosymmetric rhombohedral structural variant of $Mg_{0.5}Zr_2(PO_4)_3$ is shown in Fig. 3(b). From the FPMD calculations, it is evident that ionic diffusion was more feasible in a rhombohedral structure as compared to that in the β-Fe_2SO_4 structure, and it exhibited lower activation energy of 0.63 eV. Further, the computational studies confirmed that three-dimensional conduction occurred in the rhombohedral structure, similar to that in the monoclinic structure. Such characteristics are identical to the ionic transport observed in sodium-based NASICON compounds, where stabilizing the rhombohedral structure enhances the net ionic conduction of the material.[71] Unfortunately, there has been no experimental evidence, so far, on the synthesis of pure $Mg_{0.5}Zr_2(PO_4)_3$ with a rhombohedral crystal structure. Nevertheless, the authors do suggest that the rhombohedral structure may be stabilized in $Mg_{0.5}Zr_2(PO_4)_3$ by thin-film synthesis or doping since the energy difference in the phase stabilities of both the structures was found to be only around 14 meV per atom.[70] Indeed, in another experimental study, by partially introducing Hf^{4+} ions in the Mg^{2+} site in the above composition, the monoclinic structure transformed into a rhombohedral structure (associated with the space group $R\bar{3}c$, close to the NASICON structure), leading to ionic conductivity of 2.1×10^{-6} S cm^{-1} at 300 °C and activation energy of 0.66 eV for the optimized composition of $(Mg_{0.1}Hf_{0.9})_{4/3.8}Nb(PO_4)_3$.[72] This could further vouch for the significance of a rhombohedral structure, as seen earlier, toward the improved diffusion of magnesium ions in such structures.

$Mg_{0.5}Zr_2(PO_4)_3$—the base structure—presents opportunities for substituting aliovalent ions at the Zr- and P-sites to accommodate more magnesium ions in the structure. Several dopants such as Zn^{2+}, Al^{3+}, Fe^{3+}, Si^{4+}, Ce^{4+}, and Nb^{4+} have been studied, yielding different results.[72–84] The complete replacement of Zr^{4+} by Si^{4+}, with the $Mg_{0.5}Si_2(PO_4)_3$ composition, led to the same monoclinic structure as that in $Mg_{0.5}Zr_2(PO_4)_3$, but with much higher ionic conductivity of 1.06×10^{-6} S cm^{-1} (ref. 75) at room temperature (*vs.* 5×10^{-13} S cm^{-1} at room temperature for $Mg_{0.5}Zr_2(PO_4)_3$ determined by extrapolating from the Arrhenius plot). With the material crystallizing in the same monoclinic structure, the reduction of the unit cell volume could be the reason for the increase in ionic conductivity, which provided an appropriate bottleneck size for more feasible Mg^{2+}-ion propagation. In addition, $Mg_{0.5}Si_2(PO_4)_3$ exhibited a wide electrochemical window of up to 3.2 V, which is the highest value reported so far for an inorganic-oxide-based system, although details regarding the cell assembly are missing. The temperature-dependent conductivity behavior has not been investigated for this system yet; hence, its activation energy is not known. Halim *et al.*[76] further improved the room-temperature ionic conductivity by doping $Mg_{0.5}Si_2(PO_4)_3$ with Al^{3+} ions to create more interstitial sites in the lattice, yielding a higher charge carrier concentration in the system. The resultant composition of $Mg_{0.625}Si_{1.75}Al_{0.25}(PO_4)_3$ exhibited bulk ionic conductivity of 2.78×10^{-5} S cm^{-1} at room temperature, which is more than 10 times the parent composition. However, Al doping also resulted in a reduction in the electrochemical stability window to 2.5 V.

Moving away from mainstream NASICON-based magnesium-ion conductors, a sol–gel-synthesized composite structure based on the β-$MgSO_4$:$Mg(NO_3)_2$–0.4MgO composition also exhibited relatively good ionic conductivity in the region of 2×10^{-6} S cm^{-1} at room temperature.[85] This high conductivity seems to have been facilitated by the presence of β-$MgSO_4$ in the amorphous form across the MgO particles. With a crystal structure based on trivalent-ion-conducting $Sc_2(WO_4)_3$, Mg^{2+}-ion conduction in magnesium hafnium tungstate ($Mg(Hf(WO_4)_3)$) was found to be around 2.5×10^{-4} S cm^{-1} at 600 °C associated with activation energy of 0.84 eV.[86] The ionic transport in these materials was facilitated by the alternating arrangement of Hf^{4+} and Mg^{2+} ions along the (010) direction (as shown in Fig. 4(a)), which may lead to inhomogeneity in the bond strengths in the Hf–O and Mg–O bonds. This inhomogeneity may cause a weakening in the Mg–O bonds. The alternating arrangement was further corroborated by HAADF-STEM imaging, as shown in Fig. 4(b), with each light and dark vertical line reflecting the alternating arrangement of Mg^{4+} and Hf^{4+} ions between the W interlayers.

2.1.2. Hydrides. Borohydrides were investigated for use as Mg-ion-based solid-state electrolytes. Matsuo *et al.*[87,88] employed *ab initio* calculations to study the high-temperature diffusion of magnesium ions in $Mg(BH_4)_2$, and they reported that Mg^{2+} ions located in tetrahedral cages surrounded by BH_4^- ions had limited mobility. They attributed this low mobility to strong coulombic interactions with BH_4^- ions, and they suggested that increasing the cage size by partially substituting BH_4^- ions with larger ions, such as AlH_4^-, could facilitate magnesium-ion migration. Higashi *et al.*[89] noted that Mg^{2+} ions in $Mg(BH_4)_2$ and $Mg(BH_4)(NH_2)$ exhibited an ionic-bonding character, as determined from the Bader charge on the ion, as well as the presence of large cavities that could permit the hopping of magnesium ions. Supported by the DFT data, Higashi *et al.*[89] investigated the conduction of Mg^{2+} ions in these solids. The typical crystal structure of $Mg(BH_4)(NH_2)$ is shown in Fig. 5(a), where two of the four (BH_4) units (as in $Mg(BH_4)_2$) are replaced by two amine groups to form a tetrahedral cage around the Mg^{2+} ion, forming a B_2N_2 tetrahedron. The structure consists of alternate stacking of cations (Mg^{2+}) and anions (BH_4 and NH_2) along the *c*-axis. The closest Mg^{2+}–Mg^{2+} ions are separated by

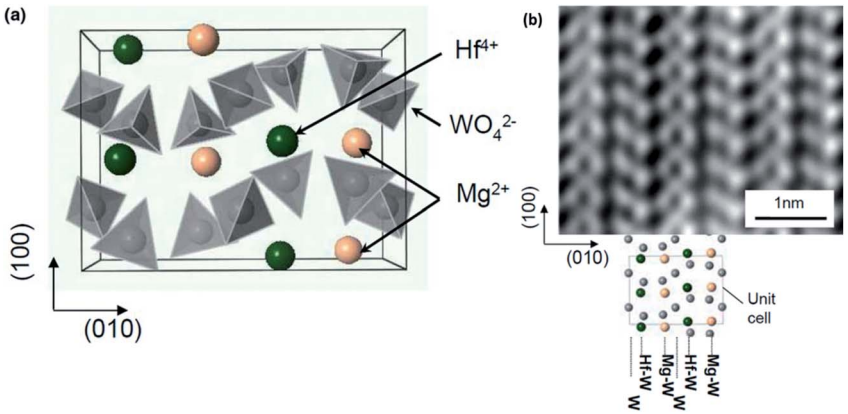

Fig. 4 (a) Structural arrangement of Mg^{2+} and Hf^{4+} between the two layers of WO_4 tetrahedra in an orthorhombic crystal structure viewed along the *c*-axis and (b) high-resolution HAADF-STEM image showing the alternating Mg^{2+} and Hf^{4+} ionic arrangement. Reproduced from ref. 86 with permission, copyright 2011, Wiley.

a distance of 3.59 Å, arranged in a peculiar zigzag fashion across the *a*–*c* plane (enlarged image, Fig. 5(a)). They reported ionic conductivity of 1×10^{-6} S cm^{-1} at 150 °C for $Mg(BH_4)(NH_2)$, which was 3 orders of magnitude higher than that of $Mg(BH_4)_2$ at the same temperature. The authors attributed this enhanced conductivity to the shorter distance between the 2 nearest magnesium atoms (3.59 Å) as compared to that in $Mg(BH_4)_2$ (4.32 Å), as well as the more pronounced ionic nature of the bonds in $Mg(BH_4)(NH_2)$. The conduction is predicted to be two-dimensional and occurs due to the migration of Mg^{2+} ions across the interstitial sites by the formation of Frenkel pairs. In addition to providing higher ionic conductivity, $Mg(BH_4(NH_2))$

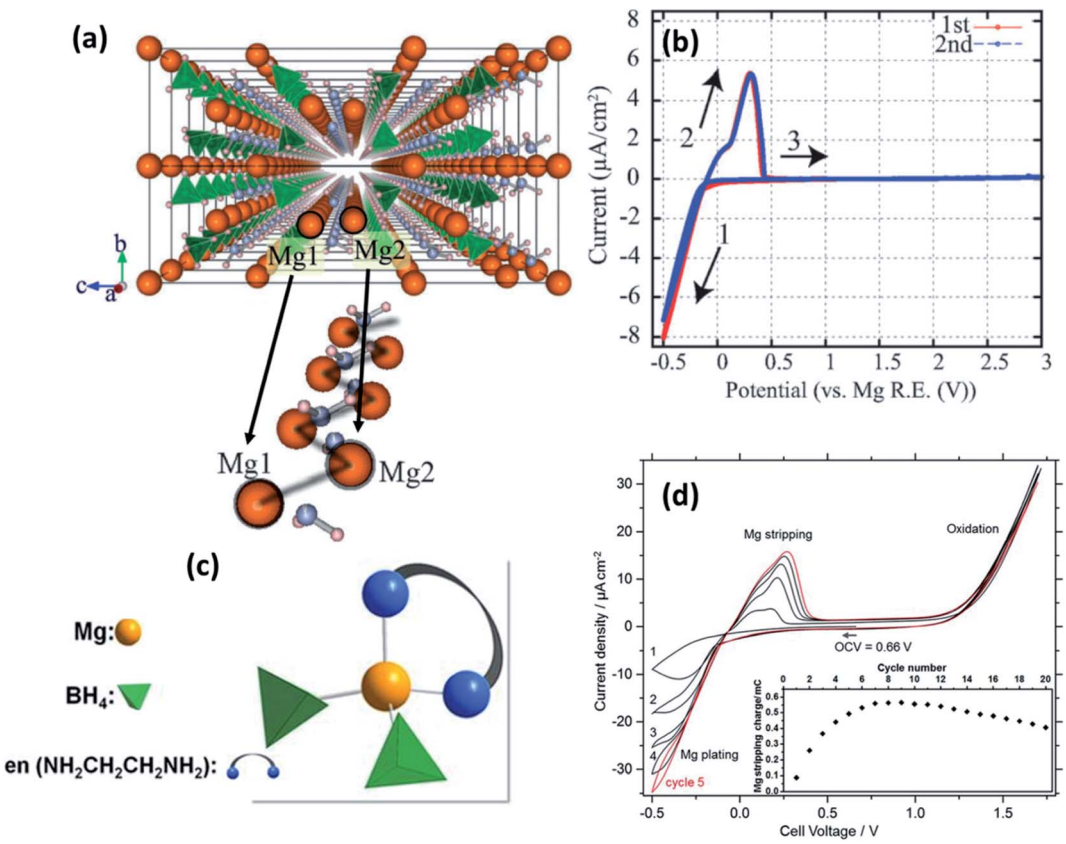

Fig. 5 (a) Crystal structure of $Mg(BH_4)(NH_2)$ viewed along the *a*-axis and an enlarged image of the Mg-ion zigzag arrangement; cyclic voltammograms of (b) Pt/$Mg(BH_4)(NH_2)$/Mg (reproduced from ref. 89 with permission, copyright 2013, Royal Society of Chemistry) and (d) Pt/$Mg(en)_1(BH_4)_2$/Mg cell at 60 °C; (c) tetrahedral arrangement of coordinating ions in $Mg(en)_1(BH_4)_2$. Reproduced from ref. 96 with permission, copyright 2017, Nature.

also exhibited the reversible plating/stripping of magnesium on Pt electrodes (Fig. 5(b)). Furthermore, the oxidative stability of $Mg(BH_4)(NH_2)$ was at least 3 V *vs.* Mg^{2+}/Mg at 150 °C. This value is higher than that of $Mg(BH_4)_2$–ether solutions at room temperature.[90] Therefore, $Mg(BH_4)(NH_2)$ seems suited for applications as a borohydride electrolyte in magnesium-based batteries operating above 150 °C.

By fine-tuning the synthesis conditions of $Mg(BH_4)(NH_2)$ (by optimizing the duration of ball milling and annealing), Le Ruyet *et al.*[91] was successful in enhancing the bulk ionic conductivity by three orders of magnitude as compared to the value reported Higashi *et al.*[89] A sample prepared by ball milling at 400 rpm followed by annealing at 120 °C for 72 h under 10 bar of hydrogen yielded ionic conductivity of 3×10^{-6} S cm^{-1} at 100 °C. Such a drastic increase in the ionic conductivity could be ascribed to the presence of a fraction of the phase in the amorphous state, which was detected by ^{11}B MAS-NMR analyses. This results in a glass–ceramic-like composite structure as the resultant product. Similar characteristics have been observed in other Li-ion glass–ceramic systems, such as $LiAlO_2$, Li_2O_2, and $LiTaO_3$, where the glass phase acts as a facile conduit for the conduction of ions.[92–95] The formation of such an amorphous phase may have been facilitated by the high-speed ball-milling process.[92–94]

Intriguingly, however, the ionic conduction in borohydrides was found to be further improved by the integration of a neutral bidentate ethylenediamine ligand ($NH_2CH_2CH_2NH_2$, "en") synthesized by the mechanical milling of $Mg(BH_4)_2$ and $Mg(en)(BH)_2$ at stoichiometric ratios in an inert atmosphere.[96] This ligand inclusion resulted in ionic conductivity in the range of 5×10^{-8} S cm^{-1} at room temperature and increased to 6×10^{-5} S cm^{-1} at 70 °C, which is a substantial improvement over those obtained from other hydrides and even several oxides. The crystal structure of this compound is unavailable at the time of writing, although by a combination of Raman and IR spectroscopies, Mg^{2+} ions were found to be coordinated by two BH_4 units and a bidentate unit in the *cis*-configuration (Fig. 5(c)). Such coordination is understood to have induced asymmetry in the charge distribution of Mg^{2+} cations, which played a role in the enhancement of ionic conductivity. However, the activation energy for ionic conduction in this compound was found to be extremely high, approximately 1.6 eV. Fig. 5(d) shows the stripping/deposition curves of Mg^{2+} ions in $Pt/Mg(en)(BH)_2/Mg$ cell recorded at 60 °C at a scan rate of 10 mV s^{-1}. The onset of magnesium plating on platinum electrodes was observed at −0.2 V *vs.* Mg^{2+}/Mg; above 1.2 V, the irreversible oxidation of the electrolyte seems to have occurred. Further, there is an improvement in the stripping/plating current density during the initial seven cycles, as shown in the inset of Fig. 5(d); thereafter, the current saturates. This behavior could be attributed to the intermediate phase, which can evidently conduct Mg^{2+} ions formed during stripping/plating due to irreversible oxidation beyond 1.2 V. It is speculated that this intermediate phase improved the interfacial connectivity between the electrolyte and electrodes. However, further investigations are needed to prove the nature of this intermediate phase.

2.1.3. Chalcogenides. One of the major breakthroughs in the search for Mg^{2+}-ion-conducting electrolytes among inorganic solids came in 2017, when Canepa *et al.*[97] discovered that $MgSc_2Se_4$ could yield high ionic conductivity of 0.1 mS cm^{-1} at room temperature, which was calculated by using first-principles calculations of the migration barriers (0.36–0.53 eV) for Mg^{2+} conduction in chalcogenide-based spinel compounds with the general formula MgX_2Z_4, where X = In, Y, or Sc and Z = S or Se. Such low migration barriers were possible because of two inherent features of these chalcogenide-based spinel structures: reduction in the coordination number of Mg^{2+} ions from 6 to 4 (from favorable octahedral to unfavorable tetrahedral sites) and increased volume per anion ($O^{2-} > S^{2-} > Se^{2-} > Te^{2-}$). Based on earlier computational studies, it was understood that faster ionic diffusion in crystalline structures can be achieved by introducing ions to unfavorable coordination in its stable site and the activated site with favorable coordination, yielding a flat energy landscape along the migration path.[98] In the case of MgX_2Z_4 spinels, Mg^{2+} ions occupy an unfavorable tetrahedral stable site and hop across a favorable octahedral activated site before reaching the next tetrahedral site along the migration path (Fig. 6(a)). This forms a *tet–oct–tet* arrangement for the migration of Mg^{2+} ions.

In normal spinel structures, the tetrahedral sites are interconnected by triangular anion cages shared across an adjacent octahedral site, and these three-coordinated anions form the ionic transport channels that influence the net activation energy of the crystal system. Therefore, it is necessary that these channels are sufficiently wide for facile ionic migration. Consequently, the size of the anion plays an important role in reducing the migration barrier. In addition to widening the ion diffusion channels, a larger anion also increases the electric polarizability of the system, which, in turn, increases the ionic conductivity of the crystal system. This variation in the migration barrier as a function of anion size can be observed, as shown in Fig. 6(b). The effect of metal cation (In, Sc, or Y) seems to be less significant and may facilitate a reduction in the energy difference between the octahedral and tetrahedral sites.

It remains imperative that spinels do not undergo any anti-site disorder or transform into inverse spinel structures, where Mg^{2+} ions occupy the octahedral sites and are connected across a vacant tetrahedral site.[97] Under these circumstances, the transport of ions occurs in the *oct–tet–oct* topology. Recent theoretical studies (based on nudged elastic band calculations) on inverse-spinel-prone $MgIn_2S_4$ systems have shown that the migration barriers across the *oct–tet–oct* topology are much higher as compared to those across the *tet–oct–tet* configuration so much so that the migration channels can be considered to be always closed.[99]

The migration barriers of Mg-based chalcogenides were determined by nudged elastic band simulation in combination with DFT, as shown in Fig. 6(b). Among these material systems, MgY_2S_4, MgY_2Se_4, and $MgSc_2Se_4$ exhibited the least migration barriers of 360, 361, and 375 meV, respectively. However, only $MgSc_2Se_4$ has been successfully synthesized and characterized so far. ^{25}Mg nuclear magnetic resonance measurements on this

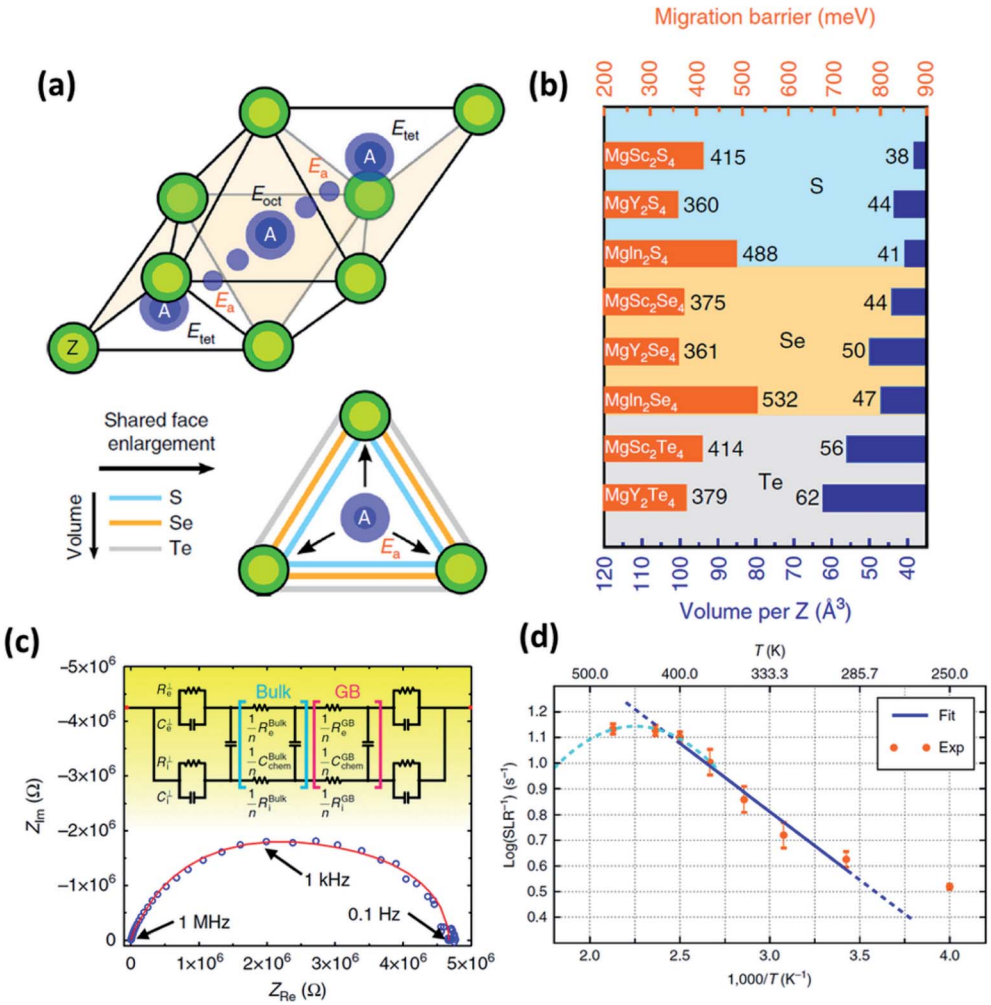

Fig. 6 (a) Migration path of Mg^{2+} ions in a MgX_2Z_4 spinel structure, where two stable tetrahedral equivalent sites are connected by a high-energy octahedral interstitial site; (b) migration barrier calculated for different magnesium spinels using first-principles calculations; (c) Nyquist plot of the Ta/$MgSc_2Se_4$/Ta cell, where the red curve signifies the equivalent circuit fitting done using Jamnik–Maier elements; and (d) spin-lattice relaxation data of ^{25}Mg recorded as a function of temperature; the blue line indicates the Arrhenius fit. Reproduced from ref. 97 with permission, copyright 2017, Nature.

compound confirmed ionic diffusion in this material from motional narrowing of the resonance peaks as a function of temperature along with the diamagnetic nature of the material. The spin–lattice relaxation was found to be very short (at 0.07–0.3 s within the temperature range, as shown in Fig. 6(d)), and the self-diffusion coefficient and activation energies were determined to be 4.53×10^{-8} cm^{-2} s^{-1} at 450 K and 0.37 eV (close to the theoretically predicted values), respectively. The high ionic conductivity of $MgSc_2Se_4$ (10^{-4} S cm^{-1} at 298 K) was determined by means of impedance spectroscopy (Fig. 6(c)) and the activation energy was estimated to be as low as 0.2 eV. Although the ionic conductivity was at a record high, this was also accompanied by high electronic conductivity ($\sim 4 \times 10^{-8}$ S cm^{-1}), as calculated from the Jamnik–Maier model of equivalent-circuit-based fitting of the Nyquist plot. This high electronic conduction may have originated from the point defects in the material that were formed as a result of Sc^{3+} ions occupying the Mg^{2+} sites, as well as the possible existence of electronically conducting secondary phases.[97,100]

Wang *et al.*[101] employed two routes to suppress the electronic conductivity in $MgSc_2Se_4$: introducing excess Se in the material and aliovalent doping of Sc^{3+} with Ti^{4+} and Ce^{4+}. The former approach seemed to be counterproductive as the addition of excess Se systematically increased the electronic conductivity from 2.1×10^{-8} S cm^{-1} at 5 wt% to 1.1×10^{-5} S cm^{-1} at 10 wt% Se. This is not surprising considering the fact that the electronic conductivity of Se is high. Therefore, any residual Se after the firing process would substantially contribute toward the increased electronic conductivity. The latter approach that involved aliovalent doping with Ti^{4+} and Ce^{4+} also yielded similar results, except for the $MgSc_{1.9}Ti_{0.075}Se_4$ composition that yielded reduced electronic conductivity of 2.7×10^{-9} S cm^{-1}. However, the authors proposed to employ selenides as the cathode material due to the combination of high ionic and electronic conductivities. The selenide cathode afforded first- and tenth-cycle

capacities of only 40 and 75 mA h g^{-1}, respectively. At any rate, exploiting this material as a cathode is limited by its high material cost and tedious processing conditions.

2.2. MOFs

MOFs feature three-dimensional permanently porous structures built around metal ions and connected through organic ligands.[102] Unlike purely inorganic solid electrolytes,[103] they are amenable to manipulation, presenting opportunities to alter their composition, pore dimensions, and internal surfaces.[104] Apart from the fact that their unique architectures permit the selective diffusion of guest species through them,[105] they can also exhibit ionic diffusivities similar to those in molten media because of the confinement effects in their small pores.[106] Moreover, unlike that in polymer electrolytes, where ionic conductivity depends on the polymer chain mobility, the conduction in MOFs occurs *via* a through-the-pore diffusion process, which implies that their conductivity and mechanical properties are not inversely proportional. MOFs are, therefore, of considerable interest for use as robust, crystalline electrolytes in the battery community.[107–109]

Aubrey *et al.*[110] reasoned that MOFs with larger concentrations of open metal sites and capable of coordinating nucleophilic anions could provide the necessary driving force for ions introduced in their pores. These pores are sufficiently large to accommodate higher concentrations of electrolytes as compared to that achievable in the bulk form. In addition, the open metal sites also inhibit the migration of anions and hence increase the transference number of the electrolyte. For MOF-based solid electrolytes, two similar frameworks with a tunable pore diameter have been considered: Mg_2(dobdc), 1, (dobdc^{4-} = 2,5-dioxidobenzene-1,4-dicarboxylate) and its expanded analog, namely, Mg_2(dobpdc), 2, (dobpdc^{4-} = 4,40-dioxidobiphenyl-3,30-dicarboxylate), as shown in Fig. 7(a) and (b), respectively. One of their electrolytes, an MOF structure of Mg_2(dobpdc) soaked in magnesium phenolates and magnesium triflates, exhibited conductivity values as high as 0.25 mS cm^{-1}. However, the only other reported Mg-ion-conducting system was based on a mesoporous anionic Cu-azolate $((CH_3)_2NH_2)[Cu_2Cl_3BTDD]\cdot(DMF)_4(H_2O)_{4.5}$ MOF that could support the diffusion of different cationic species.[111] Unfortunately, the Mg^{2+}-ion conduction in these frameworks was found to be around 8.8×10^{-7} S cm^{-1} at room temperature with the associated activation energy of 0.37 eV. This conductivity was considerably improved (up to 0.13 mS cm^{-1}) at room temperature when Miner *et al.* synthesized a solid electrolyte based on $MgBr_2$ salt in the Cu-azolate framework of $Cu_4(ttpm)_2\cdot 0.6CuCl_2$, where $Cu_4(ttpm)_2$ (H_4ttpm = tetrakis(4-tetrazolylphenyl)methane) provided multiple anion binding sites.[112]

In addition, it is imperative to estimate the Mg-ion transference number for MOF-based systems since there is a probability of protonic conduction occurring in the material due to the presence of water molecules (similar to that in Cu-azolate MOFs) or other organic functional groups.[113,114] This possibility of cationic conduction other than magnesium should be eliminated in order to determine the true value of ionic conductivities in MOFs. Information regarding the electrochemical stability window is yet to be obtained in these materials. Nevertheless, MOFs have opened a new window for research considering that not only their architecture and ligand type but also other features such as particle morphology, framework topology, and solvent polarity can influence the electrolyte properties. MOF-based electrolytes have been touted to be emerging alternatives to polymer-/ceramic-based electrolytes. Wu and Lou,[115] however, warned that the chemical/electrochemical stabilities, mechanical strength, and processability should be assessed before MOFs can be considered for commercial exploitation for use in devices. Among the variants of MOFs, Prussian blue (PB) analogs could also be explored for their use as electrolytes owing to their ability to modulate the channels to become sufficiently large for the migration of highly polarizing divalent and trivalent ions.[116] However, these materials have been predominantly researched for their use as high-voltage intercalation cathodes and are yet to step into the fold of solid electrolytes. However, if PB-based MOFs can withstand the

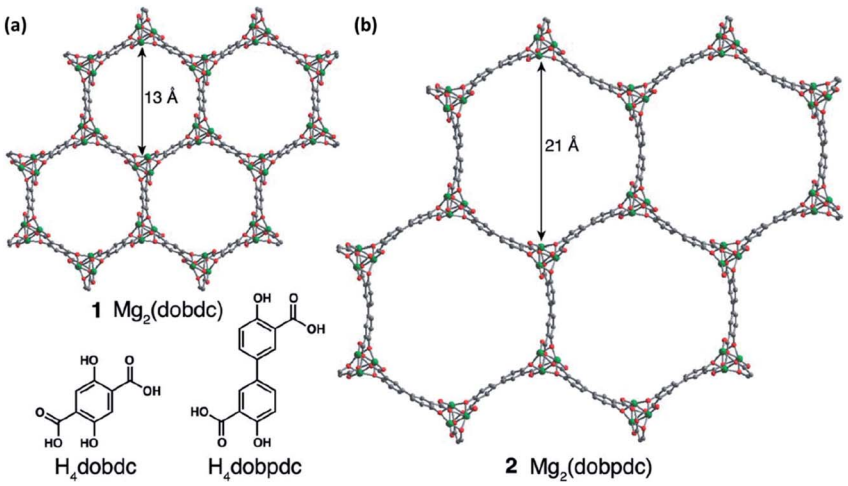

Fig. 7 Porous MOF structures of (a) Mg_2(dobdc), 1, (dobdc^{4-} = 2,5-dioxidobenzene-1,4-dicarboxylate) and (b) Mg_2(dobpdc), 2, (dobpdc^{4-} = 4,40-dioxidobiphenyl-3,30-dicarboxylate). Reproduced from ref. 110 with permission, copyright 2014, Royal Society of Chemistry.

electrochemical window of magnesium-based batteries, they can prove to be a good candidate worthy of investigation.

2.3. Glasses

The field of glasses and glass-based ceramics has come a long way since Warburg discovered ionic conduction in glasses more than a century ago. Today, glasses are one of the frontrunners in the race for fabricating an ideal electrolyte for use in all-solid-state batteries.[117–119] The ionic transport in an amorphous or disordered system is fairly different than that in its crystalline counterparts. The periodic energy landscape in a crystalline system is replaced with uneven potential wells (an approximate representation is shown in Fig. 8(a) and (b)).[120] Hence, there is a distribution of barriers for the ions to hop from one site to another, and the barrier heights are influenced by the interaction of the mobile species with the surrounding environment.

Glasses are better than crystalline materials as candidates for use as electrolytes in all-solid-state batteries because of the following advantages: absence of grain boundaries and porosity, isotropic properties, good thermal stability, negligible electronic contribution to conductivity, dimensional flexibility, and compositional tunability. Although there are several superionic conducting-glass-based materials that can conduct Li^+, Na^+, and Ag^+ ions, the field of Mg^{2+}-ion-conducting glasses is in its infancy.[121,122] In a recent study on the Mg-based analogs of Li_2S–P_2S_5 glasses, Yamanaka *et al.*[123] discussed the ionic conductivity of MgS–P_2S_5–MgI_2 glasses synthesized by a mechanochemical technique. The parent composition of $60MgS$–$40P_2S_5$ exhibited ionic conductivity in the region of $\sim 10^{-10}$ S cm^{-1} at 200 °C, which was drastically improved by 2 orders of magnitude (4.3×10^{-8} S cm^{-1} at 200 °C) by the addition of MgI to the glass network. This was understood based on the expansion of the glass network by the inclusion of a larger anion in the form of iodine, resulting in larger channels for ionic transport. Interestingly, the heat treatment of these glasses led to the precipitation of nanocrystalline $Mg_2P_2S_6$, which further increased the bulk ionic conductivity to 2.1×10^{-7} S cm^{-1} at 200 °C. The variation in the ionic conductivity as a function of the amount of MgI in glass is shown in Fig. 8(c). However, more work is needed to formulate better Mg^{2+}-ion-conducting glass. Therefore, the major impetus is toward the development of better conducting-glass-based magnesium-ion-based solid electrolytes. There is some hope from magnesium phosphorus oxynitride thin films, which are similar to their lithium counterpart, LiPON, which has ionic conductivity of 1.3×10^{-6} S cm^{-1} at 210 °C associated with the activation energy of 1.3 eV.[124]

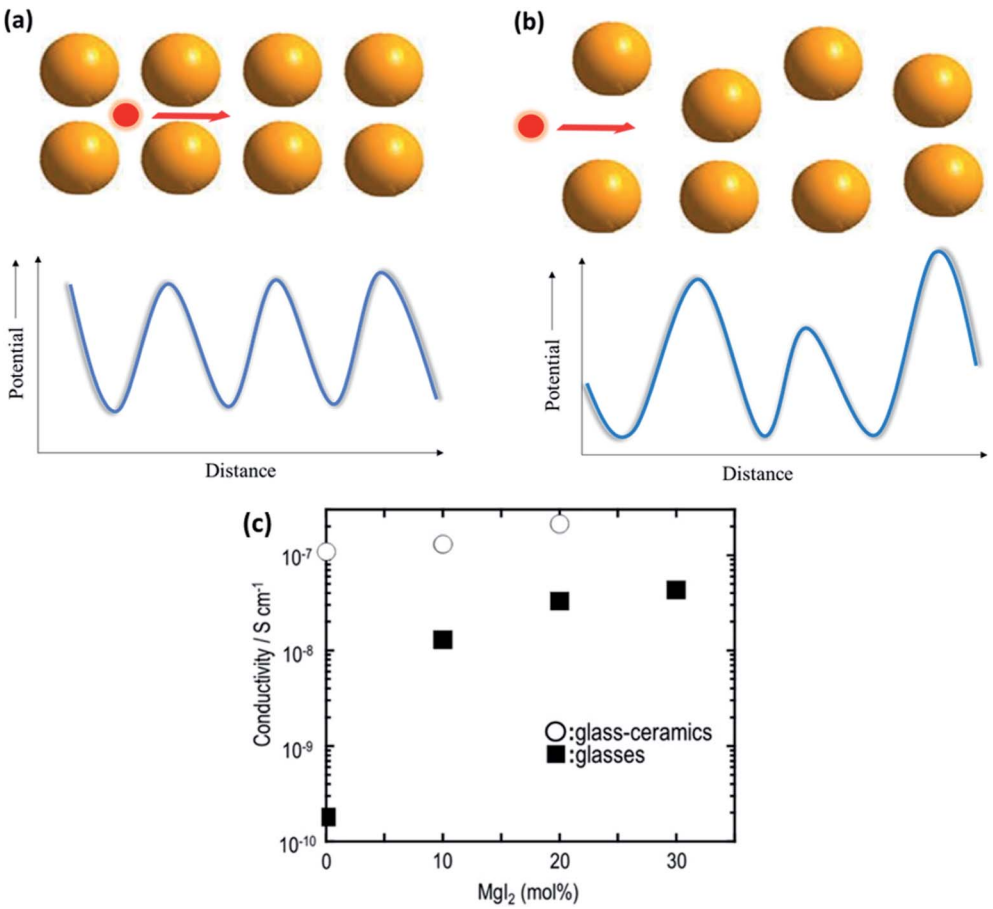

Fig. 8 Potential energy landscape for (a) crystalline and (b) amorphous materials for the transport of ions; (c) plot of ionic conductivity as a function of MgI_2 concentration in $60MgS$–$40P_2S_5$ parent glass. Reproduced from ref. 123 with permission, copyright 2014, Elsevier.

2.4. Polymer-based solid electrolytes

Because of their mechanical flexibility, low weight, and ease of processing, polymers can add a different dimension to the research on solid-state electrolytes. Polymer electrolytes are primarily categorized into solid, gel, and composite polymer electrolytes. Solid polymer electrolytes (SPEs) comprise a mobile-ion-containing salt dissolved in the polymer that forms a complex with the crosslinked chains. However, SPEs afford low ionic conductivities as the conductivity in such systems is limited by the polymer chain segmental motion. In contrast, gel polymer electrolytes (GPEs) are ionic salts dissolved in plasticizers/solvents that form a gel within a polymer matrix. This results in an increase in ionic conductivity, although the mechanical strength can be reduced. GPEs have been extensively investigated for lithium battery applications.[125,126] The third category comprises composites formed by the inclusion of ceramic fillers in a polymer matrix, which will be discussed in the subsequent section.

Similar to liquid electrolytes, the ionic conductivity of polymer electrolytes depends on the ability of the salts to dissociate in the polymer electrolytes. A well-dissociated ionic complex can enable the free propagation of mobile Mg^{2+} ions across the polymer. Ionic conduction in polymeric systems occurs as a consequence of segmental motion of the polymer chains.[127] Amorphous regions of the polymer chains create space for ions to migrate across the polymer by continuous hopping from one chain to another that is coordinated by polar groups present in the polymer. The crystalline regions, on the other hand, block the propagation of ions due to the restricted motion of polymer chains. Therefore, GPEs exhibit higher ionic conductivity than SPEs, as the crystallization of the polymer network is suppressed in the gel, which increases the ionic conductivity. The salt concentration is another defining factor that improves the net ionic conductivity. A higher content of ionic salt results in reduced ionic dissociation and adversely affects polymer chain motion, leading to reduced ionic conductivity. Hence, it is important to optimize the salt concentration in the polymer electrolyte for achieving higher ionic conductivity. However, Jeong *et al.* suggested that the Mg^{2+}-ion-conduction mechanism, which is decoupled from the segmental motion of polymer chains, is facilitated by the presence of large ionic aggregates (size: 500 nm) in the SPE system.[128]

SPE formation depends on the solvation energy and difference between the lattice energies of the ionic salt and polymer. Minimal lattice energies of the constituents are preferred for better stability of the SPE. Polymer electrolytes employ a combination of salts with polymer matrices such as polyethylene oxide (PEO), polyethylene glycol (PEG), polyvinylidene difluoride (PVDF), polymethyl methacrylate (PMMA), and polyacrylonitrile (PAN). Examples of typical salts are magnesium perchlorate ($Mg(ClO_4)_2$), magnesium trifluoromethyl sulfonyl imide ($Mg[(CF_3SO_2)_2N]_2$), magnesium triflate ($Mg(CF_3SO_3)_2$), and magnesium chloride ($MgCl_2$).[129–145] Thin films of polymer electrolytes can be fabricated *via* two common techniques: solution-cast method and hot-press technique. The former technique requires the dissolution of a polymer and an ionic salt (with or without a plasticizer) in a common solvent, which are subsequently dried in a vacuum. In the second technique, a dry homogeneous mixture of a polymer, salt, and/or filler ceramic material is heated to a temperature close to the melting point of the polymer and pressed between metal plates/twin rollers to yield thin films (in the range of micrometers).

The variation in the ionic conductivity as a function of temperature for various GPEs is shown in Fig. 9. In several polymer electrolyte systems, the Arrhenius plot of conductivity as a function of temperature assumes a convex shape rather than a single line. This is due to the temperature-dependent relaxation processes that occur owing to the polymer chain motion. One of the earliest papers on polymer electrolytes appeared in 1986 in which the room-temperature ionic conductivities of 10^{-6} and 10^{-10} S cm^{-1}, respectively, were reported for perchlorates and thiocyanates complexed with PEO.[142] This was soon followed by a blend of $MgCl_2$ in PEO, which yielded low ionic conductivity of around 10^{-9} S cm^{-1} and a negligible transference number (~0.005).[141] However, these

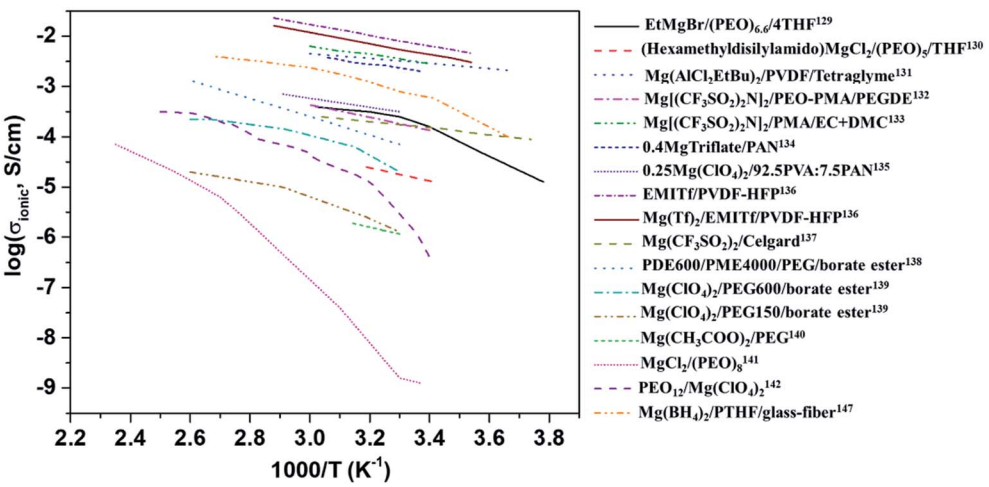

Fig. 9 Plot of variations in the ionic conductivities as a function of temperature for various polymer electrolytes.

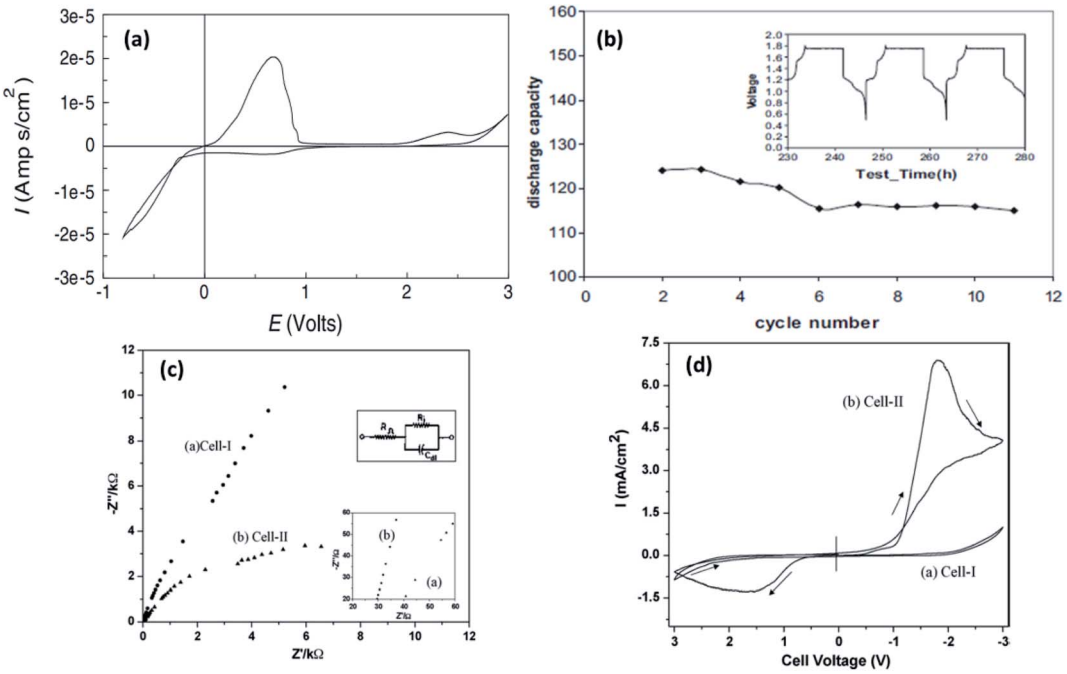

Fig. 10 Cyclic voltammetric curve recorded for Au/PVDF-Mg(AlEtBuCl$_2$)$_2$-tetraglyme/Mg; (b) plot of discharge capacity *vs.* cycle number recorded at 80 °C for a battery with Mo_6S_8 cathode, PVDF-Mg(AlEtBuCl$_2$)$_2$-tetraglyme solid electrolyte, and AZ-31 Mg alloy anode (inset shows the voltage–time curve for the same battery). Reproduced from ref. 131 with permission, copyright 2003, Elsevier; (c) Nyquist plots and (d) cyclic voltammograms of cell 1 (SS|EMITf-PVDF-HFP|SS) and cell 2 (Mg|EMITf-PVDF-HFP|Mg) recorded at room temperature. Reproduced from ref. 136 with permission, copyright 2009, Wiley; inset in (c) shows the enlarged high-frequency region of the Nyquist plot.

salts are incompatible with magnesium-metal electrodes, rendering their use as a solid electrolyte futile.

Liebenow[129,143] fabricated the first polymer electrolyte using a magnesium-metal-compatible Grignard reagent (ethyl magnesium bromide, EtMgBr) dissolved in PEO plasticized with small amounts of diethyl ether or tetrahydrofuran. The highest ionic conductivity exhibited by these polymer electrolytes was up to 10^{-4} S cm^{-1} at 40 °C.[143] The stability of the salt with respect to magnesium metal is also crucial. Chusid *et al.*[131] chose to immobilize electrolyte solutions of magnesium organohaloaluminates, such as Mg(AlCl$_2$EtBu)$_2$, in tetrahydrofuran and tetraglyme in the polymer matrices of PEO and PVDF. The plasticizers used in these systems helped soften the polymers. The authors successfully demonstrated the reversible deposition/stripping of magnesium on Au electrodes from both PEO- and PVDF-based polymer systems. The highest ionic conductivity (3.7 mS cm^{-1} at 25 °C) and the widest electrochemical window (2.5 V) were exhibited by the Mg(AlCl$_2$EtBu)$_2$/tetraglyme/PVDF system; its cyclic voltammetric curve is shown in Fig. 10(a). It is reassuring that the electrolyte is not only compatible with magnesium metal but also supports the reversible intercalation of magnesium in Chevrel-phase Mo_6S_8 with room-temperature capacity of 80 mA h g^{-1} (theoretical capacity: 122 mA h g^{-1}). Understandably, the capacity is dependent on temperature. It is noteworthy that capacity close to the theoretical value could be realized at 60 °C (Fig. 10(b)). The cyclability of an Mg-alloy/Mg(AlCl$_2$EtBu)$_2$-tetraglyme-PVDF-electrolyte/Mg$_x$Mo$_6$S$_8$ system between 0.9 and 1.2 V is shown in Fig. 10(b).

Yoshimoto *et al.*[133] showed that ionic conductivity as high as 2.8×10^{-3} S cm^{-1} at room temperature could be achieved with Mg[(CF$_3$SO$_2$)$_2$N]$_2$ dissolved in a PEO-PMMA polymer matrix plasticized with ethylene carbonate and dimethyl carbonate. As mentioned earlier, the dissociation of ions defines the ionic conductivity in a gel-based polymer system; hence, the popular inclusion of borate ester was performed by Saito *et al.*,[139] who reported not only enhanced net ionic conductivity but also improved Mg^{2+}-ion transference number (>0.50). The borate ester group closely holds together the anions in the polymeric system, facilitating the increased propagation of Mg^{2+} ions, as reflected in the increased ionic conductivity and higher transference number. The highest ionic conductivity of 4.8×10^{-3} S cm^{-1} at room temperature, comparable to that of liquid electrolytes, was achieved with a blend of 1-ethyl-3-methylimidazolium trifluoromethanesulfonate (EMITf) and magnesium triflate in poly(vinylidene fluoride-*co*-hexafluoropropylene) (PVDF-HFP), with a relatively low transference number of 0.26.[136] The electrochemical window of the GPE was determined to be 3.5 V. By using two symmetric electrode set-ups—one with stainless steel (cell 1) and the other with magnesium metal (cell 2), the ionic conductivity of the electrolyte was determined from the low-frequency tail and semicircular arc in the impedance plots (Fig. 10(c)) from cells 1 and 2, respectively. Further, the impedance plots reveal the internal resistance (see inset in Fig. 10(c)). For cell 2, the internal resistance was around 6 kΩ cm^2 as compared to that of 80 kΩ cm^2 for cell 1. Cyclic voltammograms show that this GPE supports the stripping/deposition of magnesium (Fig. 10(d)).

Such high internal resistances, sometimes called interfacial resistance, could result in the fast decay of specific capacity of a solid-state battery. This has been the characteristic of several other magnesium-based polymer electrolytes and is relatively higher than the values reported for lithium-metal/polymer cells. The internal resistance in polymer-based solid electrolyte cells has been understood to be caused by surface films by the accumulation or decomposition of charges across the cathode–electrolyte interface, and the resistance is induced by charge transfer.[146] Internal resistance may also be influenced by improper contact between the electrolyte and electrodes. For better cyclability in a battery, it is imperative that the internal resistance is kept to a minimum. The interfacial resistance arising between the electrolytes and electrodes can lead to poor cycling efficiency even in polymer electrolytes with superior ionic conductivities and wider electrochemical windows.[167,170]

In 2019, Du *et al.*[147] demonstrated a GPE formed by the *in situ* crosslinking of $[Mg(BH_4)_2]$ and hydroxyl-terminated polytetrahydrofuran (PTHF) in a glass-fiber-membrane support structure. In this composition, the high basicity of $Mg(BH_4)_2$ was circumvented by the reaction of BH_4^- and hydroxyl-terminated PTHF. A schematic of the synthesis of PTHF-borohydride-based GPE is shown in Fig. 11(a). To obtain low overpotential and enhanced electrochemical performance, $MgCl_2$ was employed as the intermediary that forms a chloride complex with borohydride without altering the magnesium coordination and without affecting the BH_4^- anion. Owing to the reduced mechanical strength of GPE after the crosslinking process, the material was infiltrated into a glass fiber membrane, which, in turn, provides strength and good flexibility. With the optimum composition of the GPE–glass fiber system, the maximum ionic conductivity of 4.76×10^{-6} S cm^{-1} could be obtained at room temperature. In addition, this material exhibited a high transference number of 0.73 at room temperature. An excellent electrochemical performance was noted with this GPE when it was used with Mo_6S_8 cathode and magnesium-metal anode: a gradual decrease in overpotential with cycling (Fig. 11(b)–(d)); 0.1C capacity of 80.6 mA h g^{-1} and 1C capacity of 66.9 mA h g^{-1} (theoretical capacity: 128.8 mA h g^{-1}); and near-perfect coulombic efficiency of 74 mA h g^{-1} over 250 cycles associated with 0.5C capacity (Fig. 11(e)). As shown in Fig. 11(h)–(k), a battery constructed using this GPE could power an LED in the 1.8–2.2 V range. Moreover, this battery could still operate even after splitting it into two halves, which implies the absence of electrolyte leakage under such damage.

Recent studies[148,149] involving the fabrication of single-ion-conducting GPEs (transference number close to unity) have yielded block copolymers produced from the copolymerization of polyethylene glycol dimethacrylate (PEGDMA) and potassium 4-styrenesulfonyl(trifluoromethylsulfonyl)imide (KSTFSI) monomer. The resultant copolymer was subsequently swelled in an appropriate solvent (dimethyl sulfoxide (DMSO)), which is compatible with magnesium metal. The copolymer exhibited ionic conductivity as high as 0.1 mS cm^{-1} at room temperature, but the hindrance in magnesium deposition from the solvated cation remains a problem owing to the large charge transfer resistance.

2.5. Composites

As the mechanical stability of GPEs is still under investigation, attempts have been made to impart structural stability to GPEs by dispersing ceramic filler particles into the polymer matrix. This provides an apt platform for ceramic–polymer-based composite electrolytes to outperform both pure polymer and ceramic electrolytes. The composite approach can combine the advantages of the polymer phase as the matrix and the ceramic particles as the filler, which can yield a solid electrolyte with tunable physical properties. Ideally, a ceramic–polymer-based composite can help achieve better interfacial stability and increased transference number in addition to improving the bulk ionic conductivity of the material.[150,151] Based on the type of contribution of the filler to the net ionic conduction in the electrolyte, a ceramic–polymer-based composite can be categorized according to its filler material as passive (or inert) or active.

With regard to passive fillers, ceramic particles can enhance the net ionic conduction in a composite without directly conducting any mobile ions. The ionic conduction in such composites undergoes two different phases, which is a function of the composition of the filler material.[152,153] The initial addition of filler particles results in a gradual increase in the ionic conductivity until it reaches the maxima. This increase is aided by the space-charge polarization induced by the filler–polymer interface. Space charge refers to an accumulation/depletion of local, uncompensated charges in solids. It could be due to the absorption of charged species on a dielectric surface, thermal ionization, or migration (sometimes field-assisted) of point defects. Interfaces, such as grain boundaries, provide active sites for the creation and retention of space charges. Space charge can be transient or permanent, temperature-dependent, or field-sensitive depending on the nature of the interface. The interface–space charge relationship is so complex that it is often difficult to quantify its effect on the bulk electrical properties. Space charge can exert a significant influence on the ionic and electronic conductivities of nanocomposites. For example, high space-charge polarization can facilitate charge separation (*e.g.*, Mg^{2+} and ClO_4^-) in a polymer network, enhancing the ionic conductivity. Moreover, the inclusion of filler particles suppresses the crystallization of polymers, allowing large amorphous regions to provide more chains that facilitate ion transport across the electrolyte by segmental motion. However, beyond the maxima, any further addition of filler particles can lead to decreased ionic conductivity as a result of the blocking effect, *i.e.*, ionic diffusion is obstructed by the large particles residing in the matrix.

In the literature, a few reports have discussed solid-state electrolytes with the inclusion of passive fillers, such as TiO_2, B_2O_3, and SiO_2, in polymer matrices.[154–157] Although B_2O_3 and TiO_2 inclusion in gel–polymer matrices lead to good ionic conduction at room temperature (7.16×10^{-6} S cm^{-1} and 5.01×10^{-5} S cm^{-1}, respectively),[154,155] SiO_2 seems to outperform with much better properties. Song *et al.*[156] reported the synthesis and electrochemical performance of a PEO-based gel-based polymer containing the ionic liquid 1-ethyl-3-

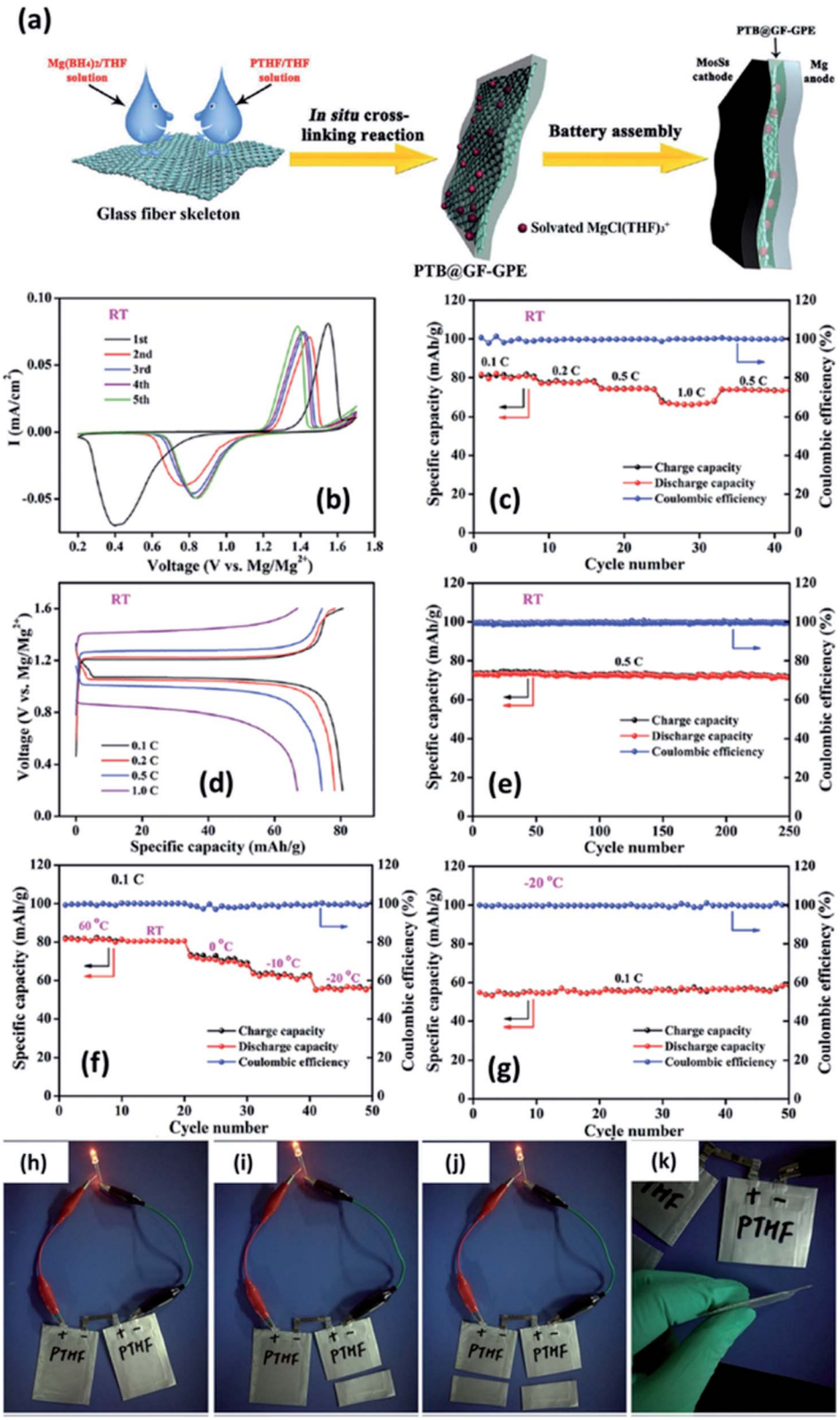

Fig. 11 (a) Schematic of the synthesis of a GPE of borohydride–polytetrahydrofuran impregnated in a glass fiber. Electrochemical characterization of a Mo_6S_8//GPE//Mg cell at room temperature (b–e) and between 60 and −20 °C (f–g). Lighting an LED using a soft-package Mo_6S_8//GPE//Mg battery (h–k). Reproduced from ref. 147 with permission, copyright 2019, Wiley.

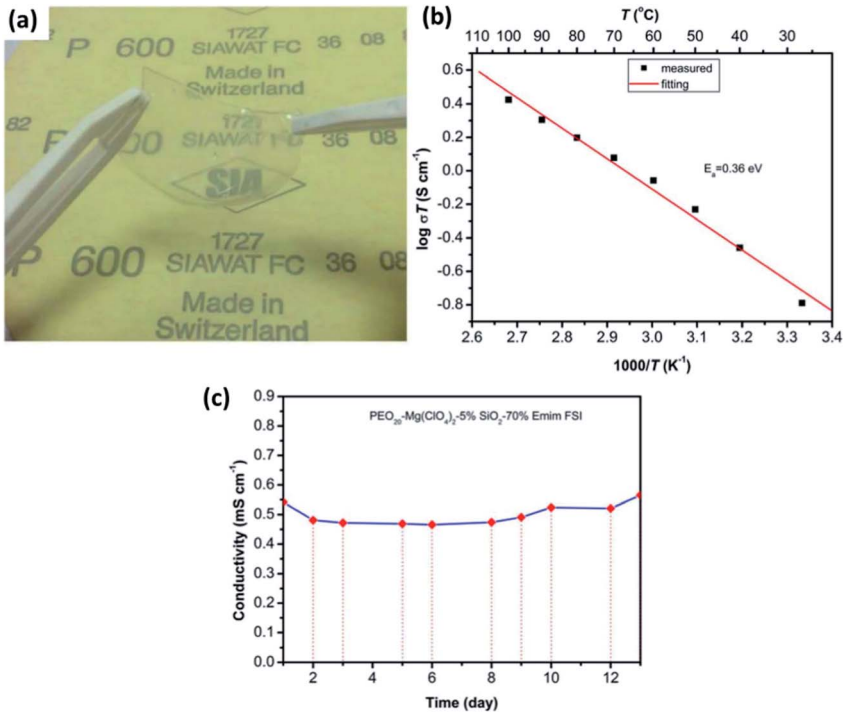

Fig. 12 (a) Photograph of a gel-based polymer system with the composition of PEO20–$Mg(ClO_4)_2$–5% SiO_2–70% EMIm, and the plots of ionic conductivity as a variable of (b) temperature and (c) time (in days) for the gel-based polymer. Reproduced from ref. 156 with permission, copyright 2017, Electrochemical Society.

methylimidazolium bis(fluorosulfonyl)imide and SiO_2 passive filler. Limiting the amount of SiO_2 to just 5 wt%, a highly flexible, free-standing, and transparent composite electrolyte could be synthesized (Fig. 12(a)). For the optimum composition of PEO20–$Mg(ClO_4)_2$–5% SiO_2–70% EMIm, these thin-film composites exhibited ionic conductivity of 5.4×10^{-4} S cm^{-1} at room temperature with the activation energy of 0.36 eV (Fig. 12(b)). Importantly, when the ionic conductivity was measured as a function of time, no decay in the conductivity was observed for as long as 12 days (Fig. 12(c)). Another enticing feature was the high electrochemical stability window of up to 4 V as measured against Mg^{2+}/Mg. Pandey *et al.*[157] developed

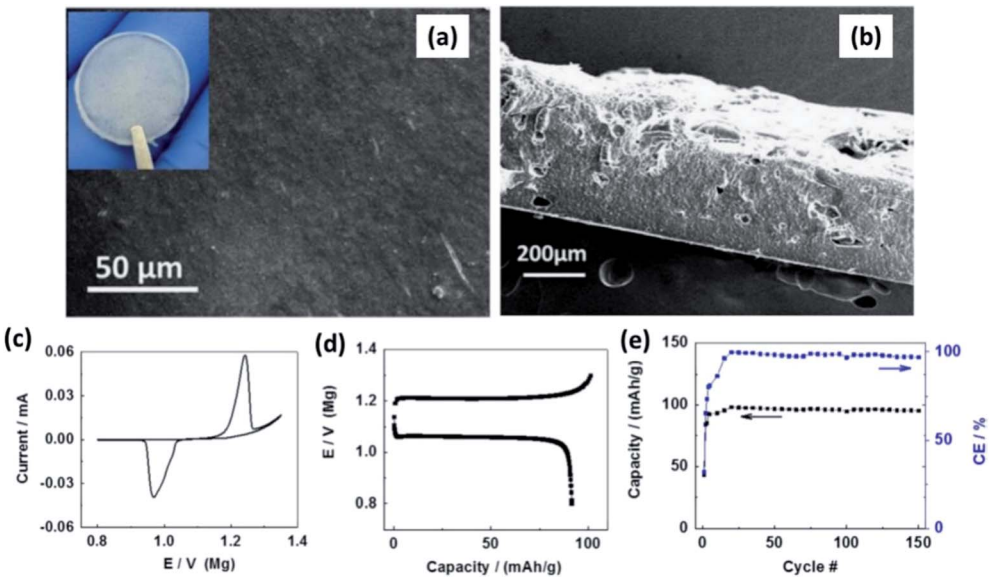

Fig. 13 SEM images of (a) the surface and (b) cross-sectional image of $Mg(BH_4)_2$–MgO–PEO nanocomposite electrolyte; (c) cyclic voltammogram, (d) charge–discharge curves, and cycling stability of the cell made using the Mo_6S_8/$Mg(BH_4)_2$–MgO–PEO/Mg arrangement. Reproduced from ref. 160 with permission, copyright 2015, Elsevier.

a composite gel electrolyte based on $Mg(ClO_4)_2$ in PVDF-HFP plasticized with polycarbonate/ethylene carbonate with fumed silica added as the ceramic filler, which exhibited very high ionic conductivity of 1.1×10^{-2} S cm^{-1}. Oh *et al.*[158] obtained ionic conductivity of 3×10^{-3} S cm^{-1} at room temperature and electrochemical stability window up to 4.3 V with a composite that had a larger content of SiO_2 in an electrolyte with the composition of 15% (PVDF-HFP)–73% $Mg(ClO_4)_2$–EC/PC–12% SiO_2.

MgO is another passive filler that has been explored in the literature. MgO is classified as a passive filler because the Mg^{2+} migration barrier in MgO is extremely high.[97] Therefore, Mg^{2+} transport across even one or two nanometers of MgO particles is unlikely at room temperature. Pandey *et al.*[159] fabricated free-standing polymer composite thin films of MgO nanoparticles (<100 nm) uniformly distributed in 1 M $Mg(ClO_4)_2$ immobilized in PVDF-HFP. This combination led to high ionic conductivity of 8×10^{-3} S cm^{-1} at room temperature with the inclusion of 10 wt% MgO. The transference number for this composition was 0.44, and bulk conductivity seemed reasonably stable over a period of 160 h. However, the voltage stability was limited to 3.5 V for 10 wt% nanocomposite. In 2015, Shao *et al.*[160] introduced a free-standing polymer composite film containing $Mg(BH_4)_2$ and PEO (1 : 8 mass ratio) with 1 wt% MgO nanoparticles. Surface and cross-sectional SEM images of the film revealed homogeneity in the distribution of ceramic fillers and absence of porosity (Fig. 13(a) and (b), respectively). The thickness of the films was 300 μm (Fig. 13(b)). With a cell containing Chevrel-phase Mo_6S_8 as the cathode, magnesium metal as the anode, and the composite electrolyte, Shao *et al.*[160] demonstrated the reversible (de)intercalation of magnesium at a sweep rate of 0.05 mV s^{-1} and showed 98% coulombic efficiency over 150 charge–discharge cycles at 100 °C (Fig. 13(c) and (d)). The difference in the onset potential for the magnesium plating and stripping was found to be as low as 0.2 V, which could imply faster kinetics. Further, the charge and discharge plateaus (Fig. 13(d)) were flat with overpotential of around 150 mV. It is noteworthy that the polymer composite did not contain any organic-based magnesium salt or ionic liquids. This possibility of magnesium intercalation using polymer composites was understood to have been aided by the dissociation of $Mg(BH_4)_2$ in the PEO matrix by the embedded MgO particles.

Till date, no significant advances in the fabrication of active-filler-embedded polymer composites have been achieved mainly due to the scarcity of highly conducting Mg^{2+}-ion ceramic materials. However, a recent report on the addition of

Table 1 Ionic conductivities, electrochemical stability windows, and Mg^{2+}-ion transference number reported for several polymer-based electrolytes for all-solid-state magnesium-based batteries

Electrolyte system	Composition	Conductivity (mS cm^{-1})	Potential window (V)	Transfer number	References
Gel polymer electrolytes	$Mg(Triflate)_2$–PVDF	2.67	3.2		161
	$Mg(Triflate)_2$–PMMA	0.42	3.3	0.55	145
	$Mg(NO_3)_2$–PEO–PVP	0.58	4	0.33	168
	$Mg(CH_3COO)_2$–PEG	1.07×10^{-3}			140
	$Mg[(CF_3SO_2)_2N]_2$–PEO–PMA–PEGDE	0.1		0.5	132
	$Mg(Triflate)_2$–PVDF-HFP–EC + PC	5.11	3.5	0.27	163
	$Mg(Triflate)_2$–PMMA–EC + DEC	0.056	2.42	0.37	166
	(Hexamethyldisilylamido)–$MgCl_2$–PEO–THF	5.2×10^{-3}	1.6		130
	$Mg(Triflate)_2$–Celgard	0.17			137
	$Mg(ClO_4)_2$–PEG–borate ester	1.25×10^{-4}		0.51	139
	$Mg(ClO_4)_2$–PDE–PME–PEG–borate ester	0.0726		0.36	138
	$Mg(ClO_4)_2$–PVA–PAN	0.296	3.65	0.27	135
	$Mg(ClO_4)_2$–PVA–PVP	0.11	3.5	0.31	169
	$Mg(ClO_4)_2$–PMMA–EC + PC	3.3		0.39	164
	$Mg(ClO_4)_2$–β-PVDF–PC	1.49	5.0	0.47	170
	$(MgTFSI)_2$–EMITfSI–PEO–PMA	0.11			171
	$Mg(AlCl_2EtBu)_2$–PVDF–tetraglyme	3.7	2.5		131
	EtMgBr–PEO–DBE	0.1	1.3		129
	$Mg(Triflate)_2$–EMITf–PVDF-HFP	4.8	3.5	0.26	136
	$Mg(Triflate)_2$–EMITf–PVDF-HFP–succinonitrile	4.0	4.1		167
	$Mg(Triflate)_2$–BMIMTf–P(VdF-HFP)	4.0			162
	$Mg(Triflate)_2$–EMITf–PEO	0.56		0.45	165
	$Mg[(CF_3SO_2)N]_2$–EC + DMC–PEO–PMA	2.8			133
	$Mg(Triflate)_2$–PC + EC–PAN	3.5	3.7		134
	$MgCl_2$–$Mg(BH_4)_2$–PTHF_glass fibres	0.476	2.5	0.73	147
Ceramic–polymer composite electrolytes	$Mg(ClO_4)_2$_fumed silica–PVDF-HFP	11	3.5	0.28	157
	$Mg(BH_4)_2$_MgO–PEO		2		160
	$Mg(ClO_4)_2$_SiO_2–PVDF-HFP	3.2	4.3		156
	$MgClO_4$_MgO–PVDF-HFP	6	3.5	0.44	159
	$Mg(CH_3COO)_2$_TiO_2–PEG	0.0501		0.98	154
	$Mg(Tf)_2$_$MgAl_2O_4$–PVDF-HFP	4	3.3	0.66	172

$MgAl_2O_4$ expected to act as an active filler in $Mg(Tf)_2$-dissolved PVDF-HFP polymer system yielded high ionic conductivity (4 mS cm^{-1}) in addition to affording a high transference number of 0.66 and electrochemical window of 3.3 V under the optimized composition. However, the contribution of magnesium aluminate on ion migration as compared to any other passive filler is yet to be fully understood. With the advent of a new generation of Mg^{2+}-ion conductors, as discussed in earlier sections, there is renewed hope for a mechanically and chemically stable, highly conducting polymer–composite solid-state electrolyte. A comprehensive list of all the GPEs and ceramic–polymer-based composite electrolytes is provided in Table 1.

3. Discussion

At present, one of the major challenges in obtaining an ideal solid-state inorganic magnesium-based electrolyte lies in the ionic conductivity at room temperature. Fig. 14 shows the Arrhenius plots of the ionic conductivities of various inorganic compounds and MOFs. The activation energies determined from the Arrhenius plots are also indicated in this figure. In practical terms, it is necessary that the materials exhibit ionic conductivities close to those of liquid electrolytes (around 1 mS cm^{-1}). From the plot, it is evident that there is a scarcity of room-temperature magnesium-ion conductors. High temperature and low conductivity remain the norm for several of these compounds. The only exceptions remain $Mg_{1.05}(Zn_{0.4}Al_{0.3}Zr_{1.3})(PO_4)_3$, $MgSc_2Se_4$, and MOFs, which show acceptable room-temperature conductivity. However, in several cases of aliovalent doping, one needs to be wary of the electronic contribution to the net conductivity, as evident from their very low activation energies (<0.1 eV). The electronic conductivity in several doped $Mg_{0.5}Zr_2(PO_4)_3$ compounds has not been covered well while studying their impedance characteristics. In the case of chalcogenides, the electronic conductivity overshadows their ionic characteristics and plagues their use as solid electrolytes. MOFs appear promising, but their compatibility with magnesium metal and high-potential cathodes remains to be explored.

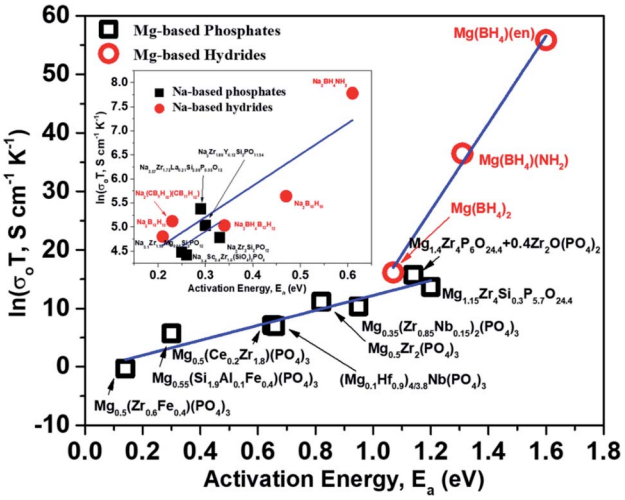

Fig. 15 Plot of prefactors as a function of activation energies for Mg- and Na-based NASICON phosphates and hydrides; the linear fit is represented by the blue lines.

To identify the limiting factor of high Mg-ion conductivity at room temperature, we performed the following analysis under the theoretical framework of multi-excitation entropy and compared the ion transport properties of several classes of Mg and Na conductors. The Arrhenius relation (as shown in Fig. 14) between the ionic conductivity (σ) of crystalline ceramics and temperature (T) is expressed as below:

$$\sigma = \sigma_o \exp\left(-\frac{E_a}{k_B T}\right) \quad (1)$$

where σ_o, E_a, and k_B are the prefactor, activation energy, and Boltzmann constant, respectively. The prefactor σ_o is a scaling factor that can be further defined by the following equation:

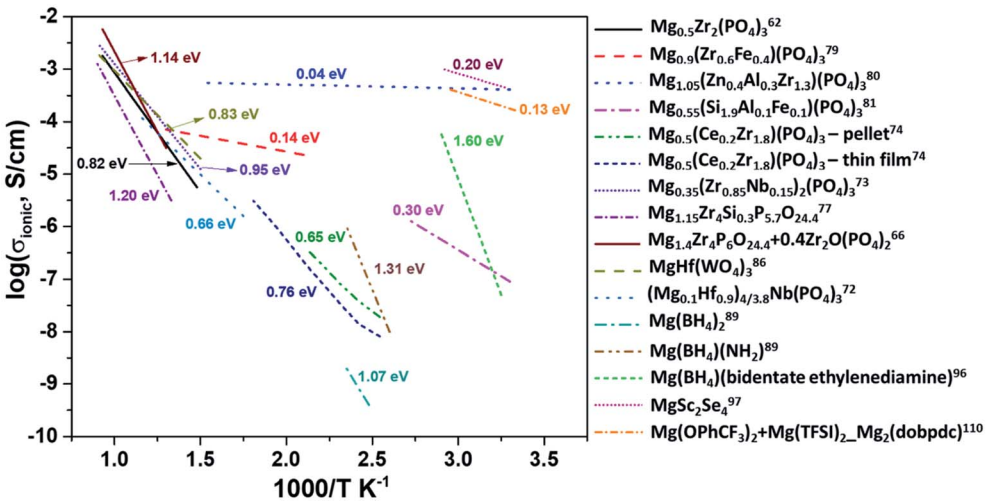

Fig. 14 Arrhenius plots of ionic conductivity as a function of the inverse of temperature for several inorganic Mg^{2+}-ion conductors.

$$\log \sigma_o = \sigma_{oo} + \left(\frac{E_a}{\Delta}\right) \quad (2)$$

where σ_{oo} is a compilation of several factors that are dependent on the carrier concentration, charge, attempt frequency of the mobile charge carriers, and jump distance; further, Δ is the annihilation energy of the phonon states that can overcome the migration barrier for ions (*e.g.*, Mg^{2+}). In some sense, the magnitude of Δ describes the strength of interaction between the phonons and ion migration. This correlation is known as the Meyer–Neldel rule.[173–178]

For a given system, a linear variation of log(prefactor) and activation energies of ion migration for a similar family of compounds can be expected based on eqn (2). Fig. 15 shows a plot of prefactors of NASICON-based pure and substituted $Mg_{0.5}Zr_2(PO_4)_3$ and borohydride-based systems as a function of their activation energies. An almost linear variation (Fig. 15) suggests that these compounds are in agreement with the Meyer–Neldel rule. The inverse of the slope from the linear fit reveals the magnitude of Δ. The extrapolated Δ values were 78 ($\pm$10) meV and 13 ($\pm$1) meV for phosphate- and borohydride-based magnesium conductors, respectively. For comparison, the prefactors (determined from earlier reported Arrhenius plots) of high-ionic-conducting sodium-based NASICON phosphates and $NaBH_4$ families of compounds were plotted as a function of their activation energies.[179–183] The Δ value obtained from the plots were found to be around 158 and 154 meV for the family of Na-based phosphates and hydrides, respectively, which are considerably higher in magnitude as compared to their Mg counterparts. These results suggest that either the phonon spectra of Mg compounds are substantially different or the interaction of lattice vibrations with Mg migration substantially varies when compared with those of their Na counterparts. The Meyer–Neldel plot calls for a tradeoff between the activation energy and prefactor in the design of improved Mg-ion conductors. Future research efforts should be directed toward improving the understanding of lattice dynamics to yield the much-yearned Mg-based solid-state electrolytes.

4. Closing remarks

Rechargeable magnesium-ion batteries are at a critical point in our research for alternatives to lithium-ion batteries, with the emphasis on sustainability. Solid electrolytes could offer the best opportunity to propel magnesium-ion batteries to the top of energy technologies. This review considered the studies and understanding of solid electrolytes for magnesium-based rechargeable batteries from a materials perspective. Some of the important achievements and discoveries made in the field of solid-state electrolytes for magnesium-based batteries are shown in Fig. 16 in the form of a timeline. Solid Mg^{2+}-ion-conducting electrolytes—categorized as inorganic ceramics, glasses, MOFs, polymers, and ceramic–polymer-based composites—have shown considerable promise, but with a pinch of salt. The low room-temperature ionic conductivities of inorganic ceramics and glasses are the first line of challenge that precludes their use in high-power applications. Although $MgSc_2Se_4$ exhibits one of the highest room-temperature ionic conductivities, the major hurdle of tapping the electronic conductivity needs to be addressed. Next, MOFs require further studies into their chemical and thermal stabilities against magnesium metal and high-potential cathodes. In addition, the tedious processing conditions for MOFs can become a deterrent

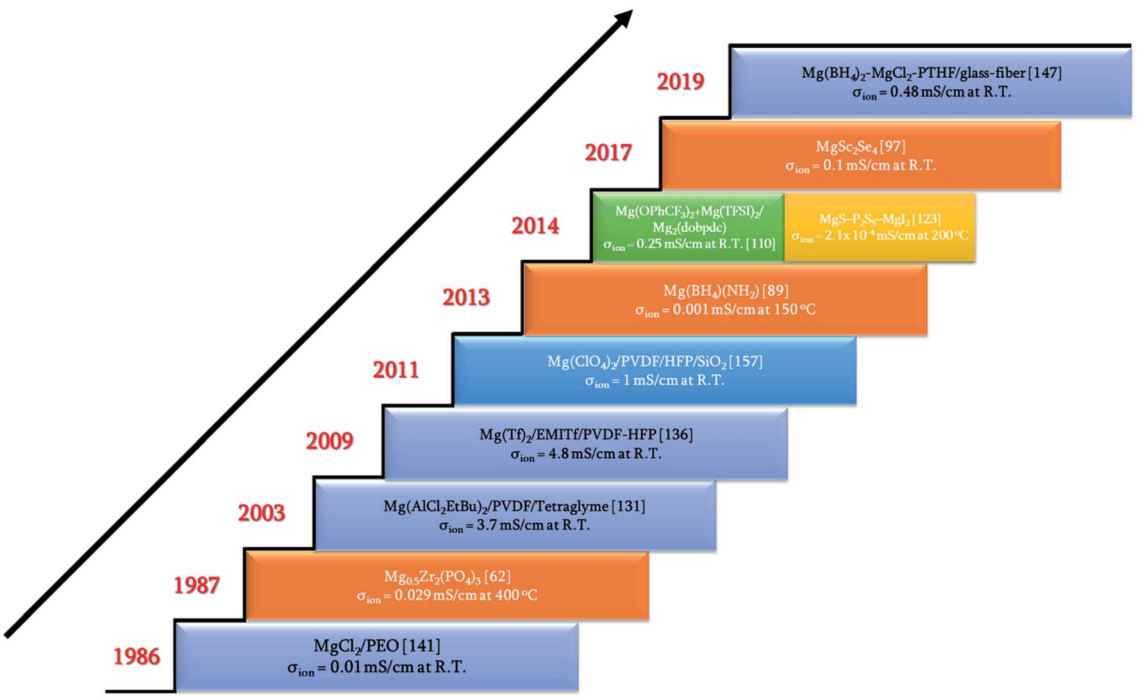

Fig. 16 Timeline of some of the breakthroughs in the search for solid-state magnesium-ion conductors.

when industrial-scale synthesis becomes a requirement. Oxides are a more economical option for solid electrolytes, and a derivative in the NASICON-based systems, namely, $Mg_{0.5}Si_2(PO_4)_3$, is the closest candidate with room-temperature ionic conductivity in the 10^{-6} S cm^{-1} range and electrochemical window of up to 3.2 V. As a side note, for a better understanding of the ionic diffusion process, concomitant detailed structural investigations to the ionic transport measurements are required. Researchers across the globe need to be encouraged to invest more in exploring the lattice structure to yield the much-yearned highly conducting Mg-based solid-state ceramic electrolytes. Polymers, on the other hand, that have been investigated have ionic conductivities close to those of their liquid counterparts, but they represent a different line of challenge: magnesium-metal compatibility and electrode–electrolyte interfacial resistance. On the other hand, recent reports on coating materials for cathodes and anodes in magnesium-ion batteries have opened up more avenues in the search for solid-state electrolytes as several of the binary, ternary, and quaternary compounds (including silicides, nitrides, borides, and oxides) exhibit low migration barriers.[184] Canepa *et al.* demonstrated that nanosizing these coating materials could help achieving desirable ionic diffusion (depending on the C-rate) in the particle even if the migration barriers are large.[185,186] This was further elaborated by identifying an Arrhenius relationship between the maximum migration barrier for high ionic diffusion and particle size. However, when these coating materials were transformed into solid electrolytes, nanosizing proved to be detrimental as it could lead to a large increase in the grain-boundary resistance, further impeding the ion transport process. The combination of low migration barrier for ionic transport, higher ionic conductivity, and better electrochemical stability, if achieved in these materials, could prove to be another breakthrough in the search for magnesium-ion-based solid-state electrolytes. Furthermore, the poor mechanical strength of solid electrolyte thin films limits the assembly only to flat cell configurations. With the present assembly protocol, based on thin-film technology, scaling up can be a challenge, too: large-sized batteries can truly become unaffordable. One school of thought to circumvent such interface issues is that in order to compete with incumbent batteries, solid-state batteries should use a "starved" electrolyte in the form of a solid pellet with a touch of liquid electrolyte so that the problems of electrode–electrolyte contact and power can be simultaneously addressed. Nevertheless, there is still a long way to go in order to realize high Mg^{2+}-ion-conducting ceramics for use in all-solid-state batteries and to reach the heights of advancements achieved by lithium-based systems.

Conflicts of interest

The authors declare no conflict of interest.

Acknowledgements

This work was supported by Shanghai Sailing Program (Contract No. 18YF1411100) and National Natural Science Foundation of China (Contract No. 51801121). One of the authors, P. W. Jaschin, acknowledges China Postdoctoral Council for the fellowship provided under the Postdoctoral International Exchange scheme. P. W. Jaschin would also like to acknowledge Dr T. Prem Kumar for useful discussions and proof-reading.

References

1 C. C. Chan, Y. S. Wong, A. Bouscayrol and K. Chen, *Proc. IEEE*, 2009, **97**, 603.
2 S. J. Skerlos and J. J. Winebrake, *Energy Policy*, 2010, **38**, 705–708.
3 B. G. Pollet, I. Staffell and J. L. Shang, *Electrochim. Acta*, 2012, **84**, 235–249.
4 A. K. Shukla and T. Prem Kumar, *J. Phys. Chem. Lett.*, 2013, **4**, 551–555.
5 (*a*) J. Axsen and K. S. Kurani, *Glob. Environ. Chang.*, 2013, **23**, 70–80; (*b*) T.-R. Hsu, *Proc. Green Energy and Systems Conf.*, Long Beach, CA, Nov. 5, 2013.
6 S. Manzetti and F. Mariasiu, *Renew. Sustain. Energy Rev.*, 2015, **51**, 1004–1012.
7 L. C. Casals, E. Martinez-Laserna, B. A. Garcia and N. Nieto, *J. Clean. Prod.*, 2016, **127**, 425–437.
8 M. A. Hannana, M. M. Hoque, A. Mohamed and A. Ayob, *Renew. Sustain. Energy Rev.*, 2017, **69**, 771–789.
9 C. Wu, W. Hua, Z. Zhang, B. Zhong, Z. Yang, G. Feng, W. Xiang, Z. Wu and X. Guo, *Adv. Sci.*, 2018, **5**, 1800519.
10 C. Wu, Z. Zhang, Y. Tang, Z. Yang, Y. Li, B. Zhong, Z.-G. Wu, X. Guo and S.-X. Dou, *ACS Appl. Mater. Interfaces*, 2018, **10**, 43740–43748.
11 C. Wu, Z.-G. Wu, X. Zhang, R. Rajagopalan, B. Zhong, W. Xiang, M. Chen, H. Li, T. Chen, E. Wang, Z. Yang and X. Guo, *ACS Appl. Mater. Interfaces*, 2017, **9**, 43596–43602.
12 C. Zhao, L. Liu, X. Qi, Y. Lu, F. Wu, J. Zhao, Y. Yu, Y.-S. Hu and L. Chen, *Adv. Energy Mater.*, 2018, **8**, 1703012.
13 P. G. Balakrishnan, R. Ramesh and T. Prem Kumar, *J. Power Sources*, 2006, **155**, 401–414.
14 R. Marom, S. F. Amalraj, N. Leifer, D. Jacob and D. Aurbach, *J. Mater. Chem.*, 2011, **21**, 9938–9954.
15 D. Lisbona and T. Snee, *Process Saf. Environ. Prot.*, 2011, **89**, 434–442.
16 J. Wen, Y. Yu and C. Chen, *Mater. Express*, 2012, **2**, 197–212.
17 B. Diouf and R. Pode, *Renewable Energy*, 2015, **76**, 375–380.
18 N. Nitta, F. Wu, J. T. Lee and G. Yushin, *Mater. Today*, 2015, **18**, 252–264.
19 S. Abada, G. Marlair, A. Lecocq, M. Petit, V. Sauvant-Moynot and F. Huet, *J. Power Sources*, 2016, **306**, 178–192.
20 J.-L. Ma, F.-L. Meng, Y. Yu, D.-P. Liu, J.-M. Yan, Y. Zhang, X.-B. Zhang and Q. Jiang, *Nat. Chem.*, 2019, **11**, 64–70.
21 Y.-D. Xu, W. Xiang, Z.-G. Wu, C.-L. Xu, Y.-C. Li, X.-D. Guo, G.-P. Lv, X. Peng and B.-H. Zhong, *Electrochim. Acta*, 2018, **268**, 358–365.
22 Y. -P. Deng, Z. -G. Wu, R. Liang, Y. Jiang, D. Luo, A. Yu and Z. Chen, *Adv. Funct. Mater.*, 2019, **29**, 1808522.
23 L. Qiu, W. Xiang, W. Tian, C.-L. Xu, Y.-C. Li, Z.-G. Wu, T.-R. Chen, K. Jia, D. Wang, F.-R. He and X.-D. Guo, *Nano Energy*, 2019, **63**, 103818.

24 F. Ding, W. Xu, G. L. Graff, J. Zhang, M. L. Sushko, X. Chen, Y. Shao, M. H. Engelhard, Z. Nie, J. Xiao, X. Liu, P. V. Sushko, J. Liu and J. G. Zhang, *J. Am. Chem. Soc.*, 2013, **135**, 4450–4456.
25 L. Gireaud, S. Grugeon, S. Laruelle, B. Yrieix and J. M. Tarascon, *Electrochem. Commun.*, 2006, **8**, 1639–1649.
26 R. S. Thompson, D. J. Schroeder, C. M. López, S. Neuhold and J. T. Vaughey, *Electrochem. Commun.*, 2011, **13**, 1369–1372.
27 J. Liu, Z. Bao, Y. Cui, E. J. Dufek, J. B. Goodenough, P. Khalifah, Q. Li, B. Y. Liaw, P. Liu, A. Manthiram, Y. S. Meng, V. R. Subramanian, M. F. Toney, V. V. Viswanathan, M. S. Whittingham, J. Xiao, W. Xu, J. Yang, X.-Q. Yang and J.-G. Zhang, *Nat. Energy*, 2019, **4**, 180–186.
28 U. Kasavajjula, C. Wang and A. J. Appleby, *J. Power Sources*, 2007, **163**, 1003–1039.
29 W.-J. Zhang, *J. Power Sources*, 2011, **196**, 13–24.
30 A. R. Kamali and D. J. Fray, *Rev. Adv. Mater. Sci.*, 2011, **27**, 14–24.
31 A. M. Chockla, K. C. Klavetter, C. B. Mullins and B. A. Korgel, *Chem. Mater.*, 2012, **24**, 3738–3745.
32 Y. Xu, Q. Liu, Y. Zhu, Y. Liu, A. Langrock, M. R. Zachariah and C. Wang, *Nano Lett.*, 2013, **13**, 470–474.
33 M. Ge, X. Fang, J. Rong and C. Zhou, *Nanotechnology*, 2013, **24**, 422001.
34 C. Wang, H. Wu, Z. Chen, M. T. McDowell, Y. Cui and Z. Bao, *Nat. Chem.*, 2013, **5**, 1042–1048.
35 Y. Zhao, X. Li, B. Yan, D. Li, S. Lawes and X. Sun, *J. Power Sources*, 2015, **274**, 869–884.
36 B. Luo, T. Q. D. Ye, L. Wang and L. Zhi, *Nano Energy*, 2016, **22**, 232–240.
37 Y. Cui and C. M. Lieber, *Science*, 2001, **291**, 851–853.
38 O. Crowther and A. C. West, *J. Electrochem. Soc.*, 2008, **155**, A806–A811.
39 D. Aurbach, Y. Cohen and M. Moshkovich, *Electrochem. Solid-State Lett.*, 2001, **4**, A113–A116.
40 M. Masaki, *J. Power Sources*, 2011, **196**, 7048–7055.
41 C. Ling, D. Banerjee and M. Matsui, *Electrochim. Acta*, 2012, **76**, 270–274.
42 R. Davidson, A. Verma, D. Santos, F. Hao, C. Fincher, S. Xiang, J. V. Buskirk, K. Xie, M. Pharr, P. Mukherjee and S. Banerjee, *ACS Energy Lett.*, 2019, **4**, 375–376.
43 T. D. Gregory, R. J. Hoffman and R. C. Winterton, *J. Electrochem. Soc.*, 1990, **137**, 775–780.
44 T. Ichitsubo, T. Adachi, S. Yagi and T. Doi, *J. Mater. Chem.*, 2011, **21**, 11764–11772.
45 D. Imamura, M. Miyayama, M. Hibino and T. Kudo, *J. Electrochem. Soc.*, 2003, **150**, A753–A758.
46 D. Imamura and M. Miyayama, *Solid State Ionics*, 2003, **173**, 173–180.
47 D. Aurbach, Z. Lu, A. Schechter, Y. Gofer, H. Gizbar, R. Turgeman, Y. Cohen, M. Moshkovich and E. Levi, *Nature*, 2000, **407**, 724–727.
48 Y. Liang, R. Feng, S. Yang, H. Ma, J. Liang and J. Chen, *Adv. Mater.*, 2011, **23**, 640–643.
49 S. Yang, D. Li, T. Zhang, Z. Tao and J. Chen, *J. Phys. Chem. C*, 2012, **116**, 1307–1312.
50 Y. Liu, L. Jiao, Q. Wu, J. Du, Y. Zhao, Y. Si, Y. Wang and H. Yuan, *J. Mater. Chem. A*, 2013, **1**, 5822–5826.
51 C. Ling and F. Mizuno, *Chem. Mater.*, 2013, **25**, 3062–3071.
52 X. Sun, P. Bonnick, V. Duffort, M. Liu, Z. Rong, K. A. Persson, G. Ceder and L. F. Nazar, *Energy Environ. Sci.*, 2016, **9**, 2273–2277.
53 Y. NuLi, J. Yang, J. Wang and Y. Li, *J. Phys. Chem. C*, 2009, **113**, 12594–12597.
54 L. Suo, O. Borodin, T. Gao, M. Olguin, J. Ho, X. Fan, C. Luo, C. Wang and K. Xu, *Science*, 2015, **350**, 938–943.
55 D. Aurbach, Y. Gofer, A. Schechter, O. Chusid, H. Gizbar, Y. Cohen, M. Moshkovich and R. Turgeman, *J. Power Sources*, 2001, **97–98**, 269–273.
56 D. Aurbach, I. Weissman, Y. Gofer and E. Levi, *Chem. Rec.*, 2003, **3**, 61–74.
57 Y. Gofer, N. Pour and D. Aurbach, Electrolytic solutions for rechargeable magnesium batteries, in *Lithium Batteries: Advanced Technologies and Applications*, Wiley-VCH, Weinheim, 2013, pp. 328–345.
58 J. Muldoon, C. B. Bucur, A. G. Oliver, T. Sugimoto, M. Matsui, H. S. Kim, G. D. Allred, J. Zajicekb and Y. Kotanie, *Energy Environ. Sci.*, 2014, **5**, 5941–5950.
59 X.-B. Cheng, R. Zhang, C.-Z. Zhao, F. Wei, J.-G. Zhang and Q. Zhang, *Adv. Sci.*, 2016, **3**, 1500213.
60 S. J. An, J. Li, C. Daniel, D. Mohanty, S. Nagpure and D. L. Wood, *Carbon*, 2016, **105**, 52.
61 C. B. Bucur, *Challenges of a rechargeable magnesium battery*, Springer Nature, Cham, Switzerland, 2018.
62 S. Ikeda, M. Takahashi, J. Ishikawa and K. Ito, *Solid State Ionics*, 1987, **23**, 125–129.
63 A. Kazakos-Kijowski, S. Komarneni, D. Agrawal and R. Roy, *Mater. Res. Bull.*, 1988, **23**, 1177–1184.
64 E. R. Gobechiya, M. V. Sukhanov, V. I. Pet'kov and Y. K. Kabalov, *Crystallogr. Rep.*, 2008, **53**, 53–59.
65 M. Adamu and G. M. Kale, *J. Phys. Chem. C*, 2016, **120**, 17909–17915.
66 N. Imanaka, Y. Okazaki and G. Adachi, *J. Mater. Chem.*, 2000, **10**, 1431–1435.
67 J. J. Didisheim, E. Prince and B. J. Wuensch, *Solid State Ionics*, 1986, **18–19**, 944–958.
68 H. Kohler and H. Schulz, *Mater. Res. Bull.*, 1985, **20**, 1461–1471.
69 K. Namura, S. Ikeda and K. Ito, *Bull. Chem. Soc. Jpn.*, 1992, **65**, 3221–3227.
70 K. Nakano, Y. Noda, N. Tanibata, M. Nakayama, K. Kajihara and K. Kanamura, *RSC Adv.*, 2019, **9**, 12590–12595.
71 Z. Zhang, Q. Zhang, J. Shi, Y. S. Chu, X. Yu, K. Xu, M. Ge, H. Yan, W. Li, L. Gu, Y.-S. Hu, H. Li, X.-Q. Yang, L. Chen and X. Huang, *Adv. Energy Mater.*, 2017, **7**, 1601196.
72 S. Tamura, M. Yamane, Y. Hoshino and N. Imanaka, *J. Solid State Chem.*, 2016, **235**, 7–11.
73 K. Kajihara, H. Nagano, T. Tsujita, H. Munakata and K. Kanamura, *J. Electrochem. Soc.*, 2017, **164**, A2183–A2185.
74 B. Liang, V. Keshishian, S. Liu, E. Yi, D. Jia, Y. Zhou, J. Kieffer, B. Ye and R. M. Laine, *Electrochim. Acta*, 2018, **272**, 144–153.

75 Z. A. Halim, S. B. R. S. Adnan and N. S. Mohamed, *Ceram. Int.*, 2016, **42**, 4452–4461.
76 Z. A. Halim, S. B. R. S. Adnan, F. M. Salleh and N. S. Mohamed, *J. Magnesium Alloys*, 2017, **5**, 439–447.
77 K. Nomura, S. Ikeda, K. Ito and H. Einaga, *Chem. Lett.*, 1992, **21**, 1897–1900.
78 N. Imanaka, Y. Okazaki and G. Adachi, *Ionics*, 2001, **7**, 440–446.
79 N. K. Anuar, S. B. R. S. Adnan, M. H. Jaafar and N. S. Mohamed, *Ionics*, 2016, **22**, 1125–1133.
80 N. K. Anuar and N. S. Mohamed, *J. Sol-Gel Sci. Technol.*, 2016, **80**, 249–258.
81 N. A. Dzulkurnain, N. A. Mustaffa and N. S. Mohamed, *J. New Mater. Electrochem. Syst.*, 2017, **20**, 135–140.
82 N. Imanaka, Y. Okazaki and G. Adachi, *Electrochem. Solid-State Lett.*, 2000, **3**, 327–329.
83 H. Takahashi and H. Takamura, *Mater. Trans.*, 2012, **53**, 932–935.
84 H. Takahashia and H. Takamura, *Key Eng. Mater.*, 2012, **508**, 291–299.
85 M. Sulaiman, N. C. Su and N. S. Mohamed, *Ionics*, 2017, **23**, 443–452.
86 A. Omote, S. Yotsuhashi, Y. Zenitani and Y. Yamada, *J. Am. Ceram. Soc.*, 2011, **94**, 2285–2288.
87 M. Matsuo, H. Oguchi, T. Sato, H. Takamura, E. Tsuchida, T. Ikeshoji and S. Orimo, *J. Alloys Compd.*, 2013, **580**, S98–S101.
88 A. Unemoto, M. Matsuo and S.-I. Orimo, *Adv. Funct. Mater.*, 2014, **24**, 2267–2279.
89 S. Higashi, K. Miwa, M. Aoki and K. Takechi, *Chem. Commun.*, 2013, **50**, 1320–1322.
90 R. Mohtadi, M. Matsui, T. S. Arthur and S.-J. Hwang, *Angew. Chem., Int. Ed.*, 2012, **51**, 9780–9783.
91 R. L. Ruyet, R. Berthelot, E. Salager, P. Florian, B. Fleutot and R. Janot, *J. Phys. Chem. C*, 2019, **123**, 10756–10763.
92 D. Wohlmuth, V. Epp, P. Bottke, I. Hanzu, B. Bitschnau, I. Letofsky-Papst, M. Kriechbaum, H. Amenitsch, F. Hofer and M. Wilkening, *J. Mater. Chem. A*, 2014, **2**, 20295–20306.
93 A. Dunst, V. Epp, I. Hanzu, S. A. Freunberger and M. Wilkening, *Energy Environ. Sci.*, 2014, **7**, 2739–2752.
94 M. Wilkening, V. Epp, A. Feldhoff and P. Heitjans, *J. Phys. Chem. C*, 2008, **112**, 9291–9300.
95 P. W. Jaschin and K. B. R. Varma, *J. Appl. Phys.*, 2017, **121**, 094101.
96 E. Roedern, R.-S. Kühnel, A. Remhof and C. Battaglia, *Sci. Rep.*, 2017, **7**, 46189.
97 P. Canepa, S.-H. Bo, G. S. Gautam, B. Key, W. D. Richards, T. Shi, Y. Tian, Y. Wang, J. Li and G. Ceder, *Nat. Commun.*, 2017, **8**, 1759.
98 Z. Rong, R. Malik, P. Canepa, G. S. Gautam, M. Liu, A. Jain, K. Persson and G. Ceder, *Chem. Mater.*, 2015, **27**, 6016–6021.
99 G. S. Gautam, P. Canepa, A. Urban, S.-H. Bo and G. Ceder, *Chem. Mater.*, 2017, **29**, 7918–7930.
100 P. Canepa, G. S. Gautam, D. Broberg, S.-H. Bo and G. Ceder, *Chem. Mater.*, 2017, **29**, 9657–9667.
101 L.-P. Wang, Z. Zhao-Karger, F. Klein, J. Chable, T. Braun, A. R. Schür, C.-R. Wang, Y.-G. Guo and M. Fichtner, *ChemSusChem*, 2019, **12**, 2286–2293.
102 J. R. Long and O. M. Yaghi, *Chem. Soc. Rev.*, 2009, **38**, 1213–1214.
103 Z. Q. Wang and S. M. Cohen, *Chem. Soc. Rev.*, 2009, **38**, 1315–1329.
104 M. Eddaoudi, J. Kim, N. Rosi, D. Vodak, J. Wachter, M. O'Keeffe and O. M. Yaghi, *Science*, 2002, **295**, 469–472.
105 F. Stallmach, S. Groger, V. Kunzell, J. Karger, O. M. Yaghi, M. Hesse and U. Muller, *Angew. Chem., Int. Ed.*, 2006, **45**, 2123–2126.
106 N. Yanai, T. Uemura, S. Horike, S. Shimomura and S. Kitagawa, *Chem. Commun.*, 2011, **47**, 1722–1724.
107 A. Morozan and F. Jaouen, *Energy Environ. Sci.*, 2012, **5**, 9269–9290.
108 L. Wang, Y. Han, X. Feng, J. Zhou, P. Qi and B. Wang, *Coord. Chem. Rev.*, 2016, **307**, 361–381.
109 H. Zhang, J. Nai, L. Yu and X. W. Lou, *Joule*, 2017, **1**, 77–107.
110 M. L. Aubrey, R. Ameloot, B. M. Wiers and J. R. Long, *Energy Environ. Sci.*, 2014, **7**, 667–671.
111 S. S. Park, Y. Tulchinsky and M. Dincă, *J. Am. Chem. Soc.*, 2017, **139**, 13260–13263.
112 E. M. Miner, S. S. Park and M. Dincă, *J. Am. Chem. Soc.*, 2019, **141**, 4422–4427.
113 J. A. Hurd, R. Vaidhyanathan, V. Thangadurai, C. I. Ratcliffe, I. L. Moudrakovski and G. K. H. Shimizu, *Nat. Chem.*, 2009, **1**, 705–710.
114 P. Ramaswamy, N. E. Wong, B. S. Gelfand and G. K. H. Shimizu, *J. Am. Chem. Soc.*, 2015, **137**, 7640–7643.
115 H. B. Wu and X. W. Lou, *Sci. Adv.*, 2017, **3**, 9252.
116 Y. Lu, L. Wang, J. Cheng and J. B. Goodenough, *Chem. Commun.*, 2012, **48**, 6544–6546.
117 T. Minami, *J. Non-Cryst. Solids*, 1985, **73**, 273–284.
118 F. Gan, *J. Non-Cryst. Solids*, 1992, **140**, 184–193.
119 A. Pradel and M. Ribes, *Mater. Sci. Eng., B*, 1989, **3**, 45–46.
120 J. C. Dyre, P. Maass, B. Roling and D. L. Sidebottom, *Rep. Prog. Phys.*, 2009, **72**, 046501.
121 F. Mizuno, A. Hayashi, K. Tadanaga and M. Tatsumisago, *Adv. Mater.*, 2005, **17**, 918–921.
122 K. Minami, A. Hayashi and M. Tatsumisago, *J. Am. Ceram. Soc.*, 2011, **94**, 1779–1783.
123 T. Yamanaka, A. Hayashi, A. Yamauchi and M. Tatsumisago, *Solid State Ionics*, 2014, **262**, 601–603.
124 Y. Nishitani, S. Shibata, T. Tsujita, O. Tetsuyuki and A. Omote, *ECS Meeting Abstr. MA2016-02*, 2016, p. 676.
125 J. Y. Song, Y. Y. Wang and C. C. Wan, *J. Power Sources*, 1999, **77**, 183–197.
126 A. M. Stephan, *Eur. Polym. J.*, 2006, **42**, 21–42.
127 C. Berthier, W. Gorecki, M. Minier, M. B. Armand, J. M. Chabagno and P. Rigaud, *Solid State Ionics*, 1983, **11**, 91–95.
128 S.-K. Jeong, Y.-K. Jo and N.-J. Jo, *Electrochim. Acta*, 2006, **52**, 1549–1555.
129 C. Liebenow, *Electrochim. Acta*, 1998, **43**, 1253–1256.
130 C. Liebenow and S. Mantey, *J. Solid State Electrochem.*, 2003, **7**, 313–316.

131 O. Chusid, Y. Gofer, H. Gizbar, Y. Vestfrid, E. Levi and D. Aurbach, *Adv. Mater.*, 2003, **15**, 627–630.
132 M. Morita, N. Yoshimoto, S. Yakushiji and M. Ishikawa, *Electrochem. Solid State Lett.*, 2001, **4**, A177–A179.
133 N. Yoshimoto, S. Yakushiji, M. Ishikawa and M. Morita, *Electrochim. Acta*, 2003, **48**, 2317–2322.
134 G. G. Kumar and N. Munichandraiah, *Solid State Ionics*, 2000, **128**, 203–210.
135 R. Manjuladevi, M. Thamilselvan, S. Selvasekarapandian, R. Mangalam, M. Premalatha and S. Monisha, *Solid State Ionics*, 2017, **308**, 90–100.
136 G. P. Pandey and S. A. Hashmi, *J. Power Sources*, 2009, **187**, 627–634.
137 S. Ikeda, Y. Mori, Y. Furuhashi, H. Masuda and O. Yamamoto, *J. Power Sources*, 1999, **81–82**, 720–723.
138 M. Saito, H. Ikuta, Y. Uchimoto, M. Wakihara, S. Yokoyama, T. Yabe and M. Yamamoto, *J. Electrochem. Soc.*, 2003, **150**, A477–A483.
139 M. Saito, H. Ikuta, Y. Uchimoto, M. Wakihara, S. Yokoyama, T. Yabe and M. Yamamoto, *J. Phys. Chem. B*, 2003, **107**, 11608–11614.
140 A. R. Polu, V. Causin, R. Kumar and R. Neppalli, *J. Korean Phys. Soc.*, 2011, **59**, 114–118.
141 L. L. Yang, A. R. McGhie and G. C. Farrington, *J. Electrochem. Soc.*, 1986, **133**, 1380–1385.
142 A. Patrick, M. Glasse, R. Latham and R. Linford, *Solid State Ionics*, 1986, **18**, 1063–1067.
143 C. Liebenow, *Solid State Ionics*, 2000, **136**, 1211–1214.
144 D. Li, X. Ji, X. Gong, F. Tsai, Q. Zhang, L. Yao, T. Jiang, R. K. Y. Li, H. Shi, S. Luan and D. Shi, *J. Power Sources*, 2019, **423**, 349–357.
145 G. G. Kumar and N. Munichandraiah, *Electrochim. Acta*, 1999, **44**, 2663–2666.
146 M. Morita, N. Yoshimoto, S. Yakushiji and M. Ishikawa, *Electrochem. Solid State Lett.*, 2001, **4**, A177–A179.
147 A. Du, H. Zhang, Z. Zhang, J. Zhao, Z. Cui, Y. Zhao, S. Dong, L. Wang, X. Zhou and G. Cui, *Adv. Mater.*, 2019, **31**, 1805930.
148 L. C. Merrill, H. O. Ford and J. L. Schaefer, *ACS Appl. Energy Mater.*, 2019, **2**, 6355–6363.
149 J. L. Thelen, S. Inceoglu, N. R. Venkatesan, N. G. Mackay and N. P. Balsara, *Macromolecules*, 2016, **49**, 9139–9147.
150 R. C. Agrawal and G. P. Pandey, *J. Phys. D: Appl. Phys.*, 2008, **41**, 223001.
151 M. Dirican, C. Yan, P. Zhu and X. Zhang, *Mater. Sci. Eng., R*, 2019, **136**, 27–46.
152 E. Bekaert, L. Buannic, U. Lassi, A. Llordés and J. Salminen, Electrolytes for Li- and Na-ion batteries: concepts, candidates, and the role of nanotechnology, in *Emerging Nanotechnologies in Rechargeable Energy Storage Systems*, ed. L. Rodriguez and N. Omar, Elsevier, Boston, 2017, pp. 1–43.
153 Z. D. Hood, H. Wang, Y. Li, A. S. Pandian, M. P. Paranthaman and C. Liang, *Solid State Ionics*, 2015, **283**, 75–80.
154 A. R. Polu, R. Kumar, K. V. Kumar and N. K. Jyothi, *AIP Conf. Proc.*, 2013, **1512**, 996–997.
155 M. Sundar and S. Selladurai, *Ionics*, 2006, **12**, 281–286.
156 S. Song, M. Kotobuki, F. Zheng, Q. Li, C. Xu, Y. Wang, W. Dong, Z. Li, N. Hu and L. Lu, *J. Electrochem. Soc.*, 2017, **164**, A741–A743.
157 G. P. Pandey, R. C. Agrawal and S. A. Hashmi, *J. Solid State Electrochem.*, 2011, **15**, 2253–2264.
158 J.-S. Oh, J.-M. Ko and D.-W. Kim, *Electrochim. Acta*, 2004, **50**, 903–906.
159 G. P. Pandey, R. C. Agrawal and S. A. Hashmi, *J. Power Sources*, 2009, **190**, 563–572.
160 Y. Shao, N. N. Rajput, J. Hu, M. Hu, T. Liu, Z. Wei, M. Gu, X. Deng, S. Xu, K. S. Han, J. Wang, Z. Nie, G. Li, K. R. Zavadil, J. Xiao, C. Wang, W. A. Henderson, J.-G. Zhang, Y. Wang, K. T. Mueller, K. Persson and J. Liu, *Nano Energy*, 2015, **12**, 750–759.
161 G. G. Kumar and N. Munichandraiah, *J. Power Sources*, 2001, **102**, 46–54.
162 S. Ramesh, S.-C. Lu and I. Vankelecom, *J. Phys. Chem. Solids*, 2013, **74**, 1380–1386.
163 A. Rosdia, N. H. Zainol and Z. Osman, *AIP Conf. Proc.*, 2016, **1711**, 050003.
164 Z. Osman, N. H. Zainol, S. M. Samin, W. G. Chong, K. B. Md Isa, L. Othman, I. Supa'at and F. Sonsudin, *Electrochim. Acta*, 2014, **131**, 148–153.
165 Y. Kumar, S. A. Hashmi and G. P. Pandey, *Electrochim. Acta*, 2011, **56**, 3864–3873.
166 S. N. Asmara, M. Z. Kufian, S. R. Majid and A. K. Arof, *Electrochim. Acta*, 2011, **57**, 91–97.
167 J. Sharma and S. A. Hashmi, *Bull. Mater. Sci.*, 2018, **41**, 147.
168 K. M. Anilkumar, B. Jinisha, M. Manoj and S. Jayalekshmi, *Eur. Polym. J.*, 2017, **89**, 249–262.
169 M. Ramaswamy, T. Malayandi, S. Subramanian, J. Srinivasalu and M. Rangaswamy, *Ionics*, 2017, **23**, 1771–1781.
170 R. Singh, S. Janakiraman, M. Khalifa, S. Anandhan, S. Ghosh, A. Venimadhav and K. Biswas, *J. Electroanal. Chem.*, 2019, **851**, 113417.
171 M. Morita, T. Shirai, N. Yoshimoto and M. Ishikawa, *J. Power Sources*, 2005, **139**, 351–355.
172 J. Sharma and S. Hashmi, *Polym. Compos.*, 2019, **40**, 1295–1306.
173 A. Dalvi, N. P. Reddy and S. C. Agarwal, *Solid State Commun.*, 2012, **152**, 612–615.
174 A. Yelon, B. Movaghar and R. S. Crandall, *Rep. Prog. Phys.*, 2006, **69**, 1145–1194.
175 D. P. Almond and A. R. West, *Solid State Ionics*, 1986, **18**, 1105–1109.
176 D. P. Almond and A. R. West, *Solid State Ionics*, 1987, **23**, 27–35.
177 K. L. Ngai, *Solid State Ionics*, 1998, **105**, 231–235.
178 S. Muy, J. C. Bachman, H.-H. Chang, L. Giordano, F. Maglia, S. Lupart, P. Lamp, W. G. Zeier and Y. Shao-Horn, *Chem. Mater.*, 2018, **30**, 5573–5582.
179 T. J. Udovic, M. Matsuo, W. S. Tang, H. Wu, V. Stavila, A. V. Soloninin, R. V. Skoryunov, O. A. Babanova, A. V. Skripov, J. J. Rush, A. Unemoto, H. Takamura and S.-I. Orimo, *Adv. Mater.*, 2014, **26**, 7622–7626.

180 Z. Zhang, Y. Shao, B. Lotsch, Y.-S. Hu, H. Li, J. Janek, L. F. Nazar, C.-W. Nan, J. Maier, M. Armand and L. Chen, *Energy Environ. Sci.*, 2018, **11**, 1945–1976.
181 J.-J. Kim, K. Yoon, I. Park and K. Kang, *Small Methods*, 2017, **1**, 1700219.
182 Q. Ma, M. Guin, S. Naqash, C.-L. Tsai, F. Tietz and O. Guillon, *Chem. Mater.*, 2016, **28**, 4821–4828.
183 S. Song, H. M. Duong, A. M. Korsunsky, N. Hu and L. Lu, *Sci. Rep.*, 2016, **6**, 32330.
184 T. Chen, G. Ceder, G. S. Gautam and P. Canepa, *Front. Chem.*, 2019, **7**, 24.
185 P. Canepa, G. S. Gautam, D. C. Hannah, R. Malik, M. Liu, K. G. Gallagher, K. A. Persson and G. Ceder, *Chem. Rev.*, 2017, **117**, 4287–4341.
186 T. Chen, G. S. Gautam and P. Canepa, *Chem. Mater.*, 2019, **31**, 8087–8099.